STRUCTURALLY ENGINEERED HIGH PERFORMANCE LAYERED OXIDE CATHODES FOR NA-ION BATTERIES

M.Tech. Thesis

By

HARI NARAYANAN VASAVAN

DEPARTMENT OF METALLURGY ENGINEERING AND MATERIALS SCIENCE
INDIAN INSTITUTE OF TECHNOLOGY INDORE
JUNE 2022

STRUCTURALLY ENGINEERED HIGH PERFORMANCE LAYERED OXIDE CATHODES FOR NA-ION BATTERIES

A THESIS

Submitted in partial fulfillment of the requirements for the award of the degree

of

Master of Technology

by

HARI NARAYANAN VASAVAN

DEPARTMENT OF METALLURGY ENGINEERING AND MATERIALS SCIENCE
INDIAN INSTITUTE OF TECHNOLOGY INDORE
JUNE 2022

INDIAN INSTITUTE OF TECHNOLOGY INDORE

CANDIDATE'S DECLARATION

I hereby certify that the work which is being presented in the thesis entitled **Structurally Engineered High Performance Layered Oxide Cathodes For Na-Ion Batteries** in the partial fulfilment of the requirements for the award of the degree of **MASTER OF TECHNOLOGY** and submitted in the **Department of Metallurgy Engineering and Materials Science (MEMS), Indian Institute of Technology Indore**, is an authentic record of my own work carried out during the time period from July 2021 to June 2022 under the supervision of Dr. Sunil Kumar, Associate Professor, MEMS department, IIT Indore.

The matter presented in this thesis has not been submitted by me for the award of any other degree of this or any other institute.

HARI NARAYANAN VASAVAN

This is to certify that the above statement made by the candidate is correct to the best of my/our knowledge.

DR. SUNIL KUMAR

HARI NARAYANAN VASAVAN has successfully given his/her M.Tech. Oral Examination held on 03 June 2022

Signature of Supervisor of M.Tech. thesis
Date: 04.06.2022

Signature of PSPC Member #1
Date: 07.06.2022

14.06.2022
Dr. A.K. Kushwaha
Signature(s) of Convener, DPGC
Date:

Signature of PSPC Member #2
Date 04/06/2022

Acknowledgements

Foremost, I owe a great debt of gratitude to my thesis supervisor Dr. Sunil Kumar, for his continuous support, patience, motivation, and enthusiasm. His valuable advice, constructive criticism, extensive discussions, and immense knowledge helped me for a fundamental understanding of the subject and accomplish my thesis. The thesis would hardly have been completed without his encouragement and persistent guidance on a daily basis throughout my M. Tech. project. I also thank him for believing in my research skill and allowing me to work on this project.

I would also like to thank my PSPC members; **Dr. Rupesh S. Devan** and **Dr. Ajay Kumar Kushwaha** , for giving their precious time for my assessment and evaluation of my work.

I am thankful to Dr. Pradeep Kumar, and Mr Deepu Kumar, IIT Mandi and Dr. Uday Deshpande, UGC-DAE CSR, Indore for providing XPS measurements.

My sincere thanks also go to **Prof. Suhas S. Joshi (Director, IIT Indore)**.

I am so grateful to Indian Institute of Technology Indore and Department of Metallurgy Engineering and Materials Science of IIT for providing me the financial support and research facilities for my M.Tech. degree.

I also want to thank my lab mates Sushmita Dwivedi, and Manish Badole for all the handy helps, technical supports, invaluable discussion and suggestions. It was a pleasant experience to work with them.

Finally, and most importantly, I want to thank my parents for their encouragement, strong support, and patience.

Hari Narayanan Vasavan

Abstract

In recent years, rapid developments in Li-ion batteries (LIBs) have made these a popular choice for secondary energy storage applications. However, as the demand for energy storage systems for mobility and portable electronics applications rises, scarcity of Li deposits and the issues related to Li recycling is expected to cause the demand for Li to exceed its supply, leading to high LIBs prices. Na-ion batteries (NIBs) are widely regarded as a possible alternative to replace LIBs to meet future demands, especially in stationary storage applications such as grid storage. This is primarily because of the comparatively natural abundance of Na and the commonalities that NIBs share with LIBs in terms of components and manufacturing techniques, paving the way for their seamless integration into the current battery eco-systems.

Cathode materials, being the primary source of ions, play a pivotal role in deciding the performance and properties of ion storage batteries. Layered oxides are considered the most attractive cathode materials for commercial Na-ion batteries because of their higher specific capacity, cyclability, and easier synthesis compared to their competitors. As most of the cathode materials used in commercial Li-ion batteries are based on the same structure, certain aspects of the research and development of these materials can be translated to the advancement of Na-ion batteries.

This thesis reports on the structural, electrical, and electrochemical properties of P2-type $Na_{0.70}Ni_{0.20}Cu_{0.15}Mn_{0.65-x}Ti_xO_2$ (NNCMT-*x* (*x* = 0, 0.025, 0.05,0.075, 0.1)) ceramic fabricated via a sol-gel method. The Rietveld refinement of the room temperature XRD diffraction data confirmed the formation of a single P2-type phase with space group $P6_3/mmc$ for the powder calcined at 850 ℃. Complex impedance spectroscopy was used to deconvolute the contributions of grains and grain boundaries to the overall conduction inside the parent material $Na_{0.70}Ni_{0.20}Cu_{0.15}Mn_{0.65}O_2$ (NNCM-0). The room temperature conductivity of the grains and grain boundaries calculated for the

NNCM-0 ceramic sintered at 1000 ℃ were estimated to be (5.25 ± 0.03) × 10^{-5} Scm^{-1} and (4.70 ± 0.05) × 10^{-6} Scm^{-1}, respectively. The respective activation energies for the grain and grain boundary conduction were 0.189 ± 0.008 eV and 0.22 ± 0.01 eV, respectively. Moreover, NNCM exhibited a sodium-ion transference number of ≈ 0.86, suggesting that the conduction in this material is dominated by the Na-ions.

Substitution with Ti^{4+} in layered oxides have been reported to stabilize the P2 structure at high voltages by forming pillars for TMO_6 slabs, reducing volume shrinkages during cycling. In the Ti substituted samples. Herein the Rietveld refinement of XRD data revealed that, in addition to the successful suppression of Na-ion vacancy ordering, Ti substitution also increased the bottleneck area of the Na-O_6 prism planes facilitating faster Na-ion conduction through the material. The SEM images showed a decrease in the aspect ratio of hexagon-type morphology of particles in Ti-substituted samples. In terms of electrochemical performance, the sample with x = 7.5% exhibited a specific capacity of 126 mAh/g at a discharge rate of 0.1C in the 2.00 - 4.25 V window, which was about 25% more than that of the undoped material. At a discharge rate of 1C, the specific capacity of $Na_{0.70}Ni_{0.20}Cu_{0.15}Mn_{0.575}Ti_{0.075}O_2$ was 97 mAh/g compared to 74 mAh/g for $Na_{0.70}Ni_{0.20}Cu_{0.15}Mn_{0.65}O_2$ sample. NNCMT samples also exhibited excellent cyclability, with over 95% of original capacity retained after 300 cycles. Complex impedance measurements corroborated the improved Na-ion conductivity in Ti-doped samples and an associated increase in Na-ion transference number from 0.86 for the sample with x = 0 to 0.97 for the sample with x = 0.075.

LIST OF PUBLICATIONS

Journal publication as first author:

1. H.N. Vasavan, M. Badole, S. Dwivedi, and S. Kumar, *Structural and transfer properties of P2-type layered oxide,* ***Ceramic International*** *(Accepted for publication).*
2. H.N. Vasavan, M. Badole, S. Dwivedi, D. Kumar, P. Kumar and S. Kumar, *Modifications In the Crystal Structure and Particle Morphology Induced by Ti Substitution in P2-Type Layered Oxide Led To Enhanced Rate Performance And Specific Capacity ,* ***Chemical Engineering journal*** *(Revised manuscript submitted after peer-review round).*

Journal publication as co-author:

1. M. Badole, S. Dwivedi, H.N. Vasavan, and S. Kumar, *The Role of Salts Selection on Phase Formation and Electrical Properties of* $K_{0.5}Bi_{0.5}TiO_3$ *Ceramics Fabricated via Molten Salt Synthesis,* ***Materials Chemistry and Physics***, 283 (2022) 126017
2. S. Dwivedi, M. Badole, H.N. Vasavan, and S. Kumar, *Influence of annealing environment on the conduction behaviour of KNN-based piezoceramics,* ***Ceramics International****, Available online (2022), doi.org/10.1016/j.ceramint.2022.02.235*
3. M. Badole, S. Dwivedi, H.N. Vasavan and S. Kumar, *poling effect on electrical properties of KBT based Piezoceramics,* ***DAE Conference Proceedings, 2022.***

TABLE OF CONTENTS

List of figures

List of Tables

Nomenclature

X-ray Diffraction	XRD
Field Emission Scanning Electron Microscopy	FESEM
Complex Impedence Spectrocsopy	CIS
X-ray Photoelectron Spectroscopy	XPS
Galvanometric Charge and Discharge	GCD
Cyclic Votammetry	CV
a, b, c	Lattice Parameters
Real part of Impedance	*Z*’
Imaginary part of Impedance	*Z*”
Conductivity	σ
Boltzman constant	k_B
Resistance	R
Capacitance	C
Constant phase Element	CPE
Na ion Transference Number	t_{Na+}
$Na_{0.70}Cu_{0.15}Ni_{0.20}Mn_{0.65}O_2$	NNCM
$Na_{0.70}Cu_{0.15}Ni_{0.20}Mn_{(0.65-x)}Ti_xO_2$	(NNCMT-*x*)

INTRODUCTION

1.1. Energy Storage System:

As energy demand steadily rises across the globe, the need for convenient forms of energy storage has become the need of the hour. Energy storage systems are vital due to the versatility of their applications. Apart from obvious reasons such as a convenient method of energy transportation and saving surplus for a time of deficiency, energy storage systems are employed in power plants to cope with demand fluctuations, temporarily control sudden surges during peak hours of demand, and power all the plant's axillary systems. The rapid fluctuations in renewable energy sources such as wind and tidal energy are also smoothened using energy storage systems. Energy storage systems are also used to provide large and rapid energy bursts from a constant power source in various applications. To sum up, storage systems make energy usable.

Energy is stored in various forms depending on its application, as shown in Fig. 1.1. Most artificial systems store energy in the form of potential, chemical, electrochemical, thermal, and mechanical energy. Among these, electrochemical energy storage systems have become the most widely used option today.

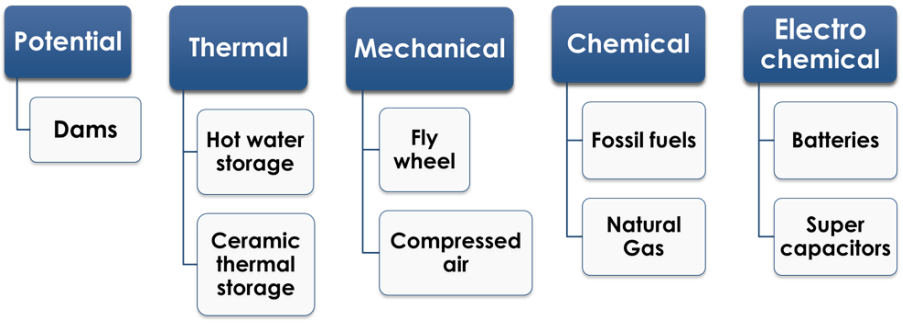

Figure 1.1. Classification of energy storage systems.

1.2. Electrochemical energy storage

Electrochemical energy storage units store electricity in a chemical form. They are more versatile and cost-effective than other storage units for small and medium-scale energy applications. These are compact and don't need energy converters. This makes them easy to store and transport. Unlike mechanical and thermal energy storage systems, they do not have any moving parts and can store energy for extended periods with little to no maintenance. Electrochemical storage systems can be manufactured in various sizes with a wide range of capacities and can still be cost-effective. These are safer and more efficient compared to many other types of storage systems; hence, these have been the subject of extensive research over the years.

Batteries, supercapacitors, and fuel cells are the most common type of electrochemical energy storage units. Batteries are self-contained energy storage units that store and provide energy at varying discharge rates for extended periods. In contrast, supercapacitors can provide high-energy bursts (more than 10 times that of batteries) for shorter periods (typically, less than 30 seconds). Fuel cells convert the chemical energy of a fuel (often hydrogen) and an oxidizing agent (usually oxygen) into electricity.

A Ragone plot best depicts the comparison between supercapacitors and batteries. A Ragone plot is a chart with specific energy (Wh/kg) being plotted versus the specific power (W/kg). Specific energy is the total usable energy inside the device, and specific power refers to the energy extracted per unit time. Typically, both quantities are plotted on a logarithmic scale in a Ragone plot making it a convenient way to compare the performance between various devices and even materials. Figure 1.2 depicts a Ragone plot comparing different energy devices. The dashed lines drawn diagonally indicate discharge times.

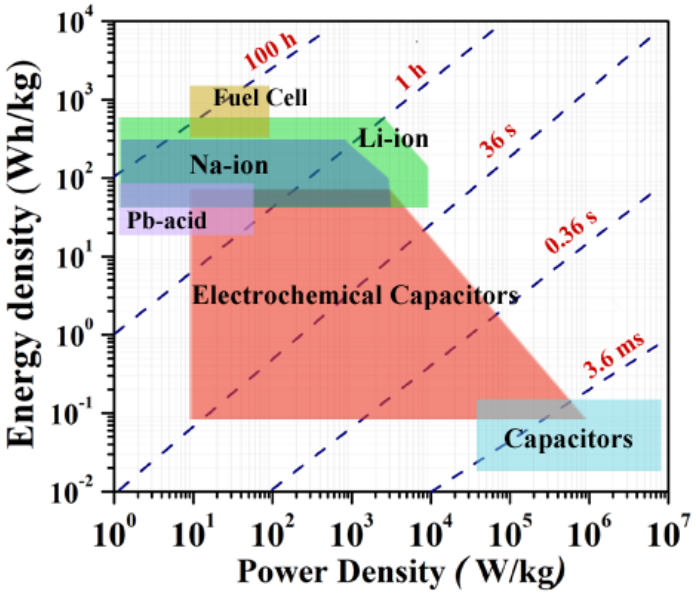

Figure 1.2. A typical Ragone plot comparing different energy storage systems. The dash blue lines indicate discharge times.

1.3. Batteries

Batteries are compact power sources that use chemical reactions to power various devices ranging from small remotes to large submarines. These can be classified into 2 types: *primary* and *secondary* batteries, as shown in Fig. 1.3. *Primary* batteries use nonreversible reactions rendering them *non-rechargeable*, and hence, these are discarded after being drained. On the other hand, *secondary* batteries use reversible reactions and can be reused after *recharging*.

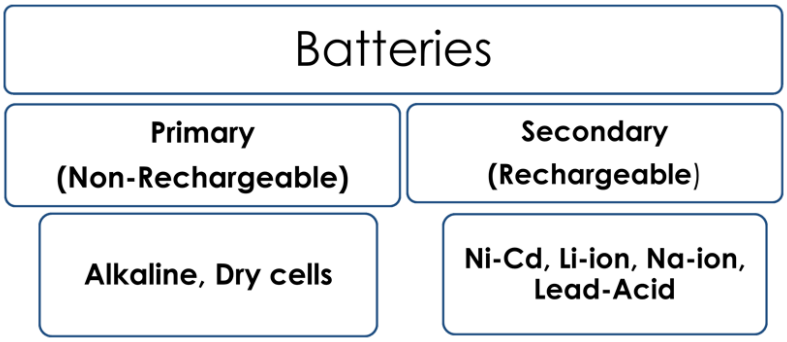

Figure 1.3. Classification of batteries.

Most of the research into batteries is concentrated on secondary batteries-based ion storage. Ion storage batteries like Li-ion batteries

are widely used in various applications due to their high energy density and superior cyclic performance.

1.4 Ion Storage Batteries

Ion storage batteries use the principle of ion storage to store charge. A battery is a combination of multiple electrochemical cells connected in series or parallel. A cell mainly consists of -

- Cathode - cathode materials either intercalate ions into their structure on discharge or de intercalate ions on charging.
- Anode - acts as a storage space for ions during charging.
- Electrolyte - Electrolytes offer very high resistance to electrons while conducting ions.
- Separator - porous membranes that are only used with liquid electrolytes to isolate the cathode and anode to prevent them from short-circuiting.
- Current collectors - electronically conductive materials on which the cathode/anode slurry is coated.

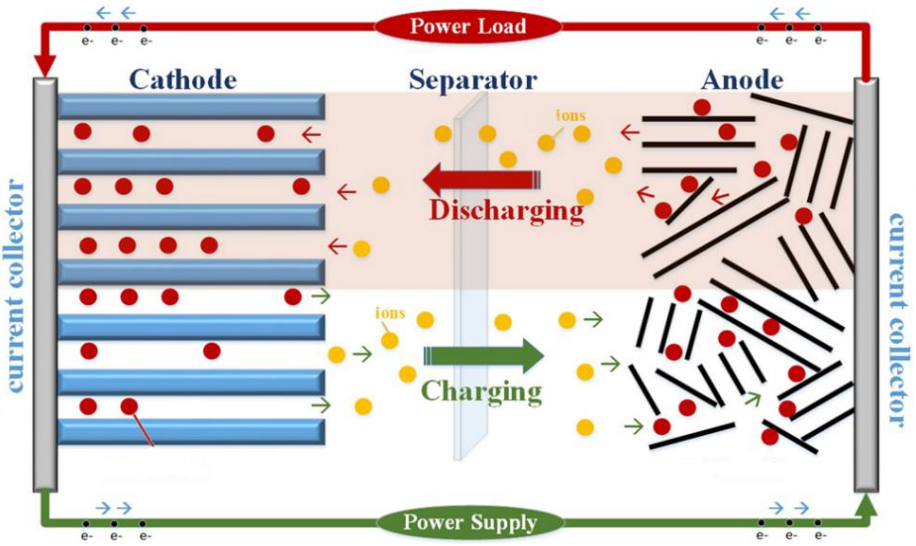

Figure 1.4. Schematic representation of an ion storage cell with potential materials listed for the electrodes and electrolyte.

Figure 1.4 shows a schematic of the working of an ion storage battery with intercalation/deintercalation type electrodes. During charging, the ions from the cathode are intercalated into the anode material while the electrons travel through the external power source from the cathode to

the anode. The reverse occurs while discharging, where the ions return to the cathode through the electrolyte while the electrons travel through the external load.

1.4.1. Li-ion Batteries (LIBs)

Li^+-based ion storage batteries use Li-ions to store energy. Currently, LIBs dominate the portable electronics (and even electric vehicles) market as the power source. These batteries have specific energies close to 150 Wh/kg and a cycle life close to 2000 cycles. LIBs enjoy a variety of advantages over other metal-ion batteries like those based on Na-ion. Li is the lightest metal; it has an ionic radius of about 0.74 Å, while Na ions are 3 times heavier and ~ 1.5 times larger. This means that Li-ions need smaller interstitials to occupy and a relatively lower volume expansion on intercalation. Li-ions, being lighter, can travel much faster through the electrolyte. The electrode potential of Li^+/Li is ~ 3.05 V *vs.* SHE (standard hydrogen electrode), and hence, Li-ion batteries can generate high energy outputs. Li-ion batteries also have higher cyclability and show lower capacity fading with time. In short, Li-ion batteries outperform all other metal-ion batteries in terms of most performance parameters.

In an ion storage battery, the cathode being the primary source of ions determine most of its performance characteristics. Li-ion batteries today use a variety of cathodes, most of which are based on layered oxides. Materials like lithium cobalt oxide ($LiCoO_2$), used in the 1990s, had an energy density of 150 Wh/kg and average cycle life of ~ 1000 cycles. Nowadays, nickel-based cathodes like lithium nickel manganese cobalt oxide ($LiNi_xMn_yCo_{(1-x-y)}O_2$) and lithium nickel cobalt aluminium oxide ($LiNi_xCo_yAl_{(1-x-y)}O_2$) with better energy densities (> 220 Wh/kg) and cycle life (> 2000 cycles) are used in mobile applications. Cathodes based on lithium iron phosphate ($LiFePO_4$, LFP) are widely used for stationary storage applications. LFP batteries have a lower energy density of ~ 100 Wh/kg but are comparatively cheaper. Graphite is often used as the anode in most

Li^+-based batteries. It can accommodate Li-ions during charging and shows a reversible capacity of ~ 350 mAh/g. Currently, China dominates the market in terms of battery production, contributing to about 78% of the total production (Fig. 1.5).

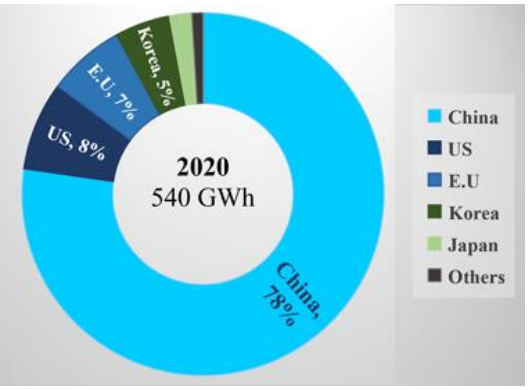

Figure 1.5. Li-ion battery production capacity by country.

1.4.2. Na-ion Batteries (NIBs)

Even though Li-ion batteries are superior in performance, these are costly and have supply chain & sustainability issues in the absence of robust recycling process. Li metal deposits make only about 0.06% of the earth's crust and are found only in a few countries. It requires about 36 MJ of energy to extract 1 kg of lithium, and the process releases about 15 tons of CO_2 for each ton of Li. In comparison, Na makes up about 2.9% of the earth's crust. It is easier & cheaper to extract and is not environmentally degrading. With Li metal deposits shrinking and an ever-increasing demand, LIBs are expected to become much more expensive in the next decade. Moreover, Li-ion-based batteries use copper as the anode current collector while aluminium is used for Na-ion batteries, making NIBs much cheaper [1, 2].

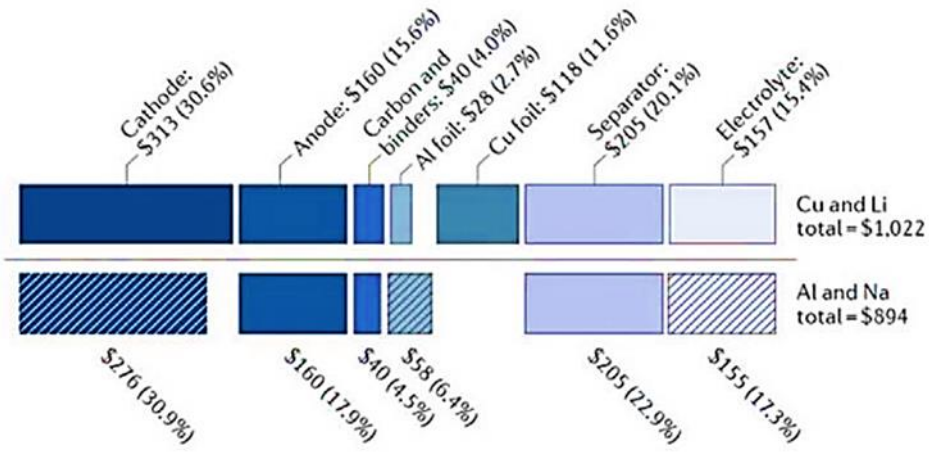

Figure 1.6. Contribution of each element towards the overall cost of Li-ion and Na-ion batteries.

The storage and transport of LIBs are regulated in most countries, which means that their transport and storage need special approvals and safety measures. NIBs fare better in terms of recyclability, too, as recycling technology for Li-ion is still in infancy with little progress in the last decade. Na-ion batteries are projected to be about 10% cheaper than LIBs (Fig. 1.6). This difference is expected to increase in the near future as NIBs become commercially available. The cost factor has made Na ions batteries attractive and many companies are planning to launch commercial NIBs within the next 2 years. Accordingly, NIBs are being extensively studied to improve their performance parameters at least on par with the LIBs, if not better [3, 4].

The challenges to integrating Na-ions in batteries come from their larger size, higher mass, and lower potential. This causes NIBs to have lower energy densities than LIBs. Only the sodium-sulphur (Na-S) and sodium metal halide batteries (ZEBRA batteries) are used commercially to replace lead-acid batteries in many stationary storage applications. Among these, Na-S batteries are more popular due to their simpler design and lower cost. Na-S batteries use a Na metal anode and sulphur cathode separated by a solid electrolyte called β"-alumina. Na-S batteries are extensively used for stationary energy

storage applications around the world. They have an energy density of 140-200 Wh/kg and generally operate at 300 ℃ [5].

As modern batteries need to be operated at room temperature, various cathode materials such as layered oxides (LOs), NASICON, and Prussian blue analogues (PBA) have been the topic of intensive research over the years. NASICON (NA Super Ionic CONductor) based cathodes show high voltages above 3.5 V and have good cyclability. However, these materials are hard to synthesise and have low specific capacities (~ 90 mAh/g). Prussian blue is a novel material based on cyanides known to have capacities above 120 mAh/g. Layered oxides are considered the most attractive cathode materials for commercial NIBs. LOs are reported to have a high specific capacity, cyclability, and easier synthesis than their competitors [6, 7].

Hard carbon is widely accepted as a suitable anode material for NIBs. With a specific capacity of 300 mAh/g, hard carbon is an amorphous form of carbon with and is capable of accommodating Na-ions.

1.4.3. Layered Oxides

Layered oxides (general formula: Na_xTMO_2; TM - transition metals) are easy to synthesize and also have high potential versus Na^+/Na. Layered oxides are already employed in Li-ion batteries, and the knowledge gained in their research can be applied to the advancement of Na-ion batteries.

Recent studies show that many transition elements that are considered inactive or degrading in Li-ion batteries are quite active and can even enhance the performance of Na-ion batteries primarily due to the larger size of Na-ions. The increased number of alternatives has kindled further research in Na-ion batteries to replace cobalt, which is considered the holy grail of cathode elements in Li-ion batteries [7, 8].

Structure

Layered oxides (LOs) based on Na have a basic formula $Na_xTMO_{2;}$ $0 \leq x \leq 1$, TM – single or a combination of transition metal cations. They are primarily found to exist in 5 phases (named based on the nomenclature developed by Delmas et al. [9]) O1, O2, O3, P2, and P3. The O and P indicate the presence of octahedral (O) or prismatic (P) coordination of oxide ions around sodium, and the numbers represent the stacking repeats of the oxygen lattice in a unit cell [10]. This is represented in Fig. 1.6. Additionally, a prime (') is added if the symmetry of a phase is distorted from the regular hexagonal or rhombohedral to monoclinic, triclinic, or orthorhombic.

P2 and P3 phases are generally found in LOs when $x < 0.8$, while the O3 phase has x almost equal 1. O3 and P2 can also reversibly transform to P3 and O2 phases, respectively, and vice versa during de-intercalation and intercalation of Na-ions through a slab glide mechanism (Fig. 1.7). Transformations from O3 to P2 are only observed at high temperatures as this requires the cleavage of metal-oxygen bonds. Transformations between O3 → O1 and P3 → O1 are also possible but are only observed in a few compounds at high voltages [11, 12].

Other types of phases such as Z and OP4 are also encountered in literature. These are derivations of the basic phases. The Z phase is a derivative of an O-type phase with some TM migration to tetrahedral sites with a significant number of stacking faults, and the OP4 phase is made up of one P-phase layer followed by one O-phase layer [13].

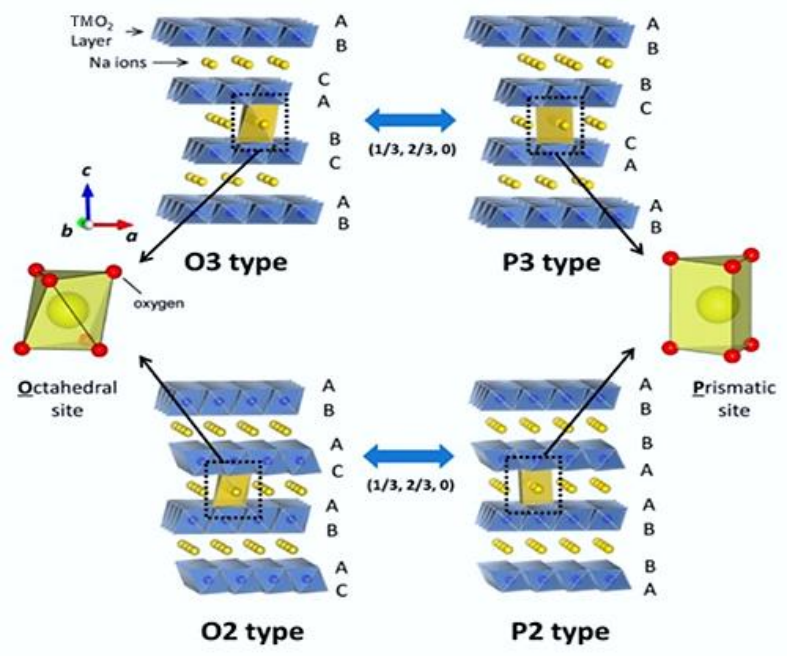

Figure 1.7. Diagram representing different layered oxide structures

Electrical Properties

P2-type materials are seen as better electrode materials compared to O3-type because of larger interlayer spacing and close-packed prismatic sites forming lower diffusion barriers leading to faster Na-ion conduction. O3-type LOs, on the other hand, have a larger Na-ions concentration, giving it a better specic capacity. P3-type LOs are rarely synthesized, and are formed during the charging of Na-ion cells with O3-type cathodes [11, 14].

P2 materials have two distinguishable trigonal prismatic Na sites, Na1 and Na2, in their structures arranged one after the other sharing a single face. The diffusion of Na-ions involves repeating $Na^1 \rightarrow Na^2 \rightarrow Na^1$ migrations. In contrast, P3-type materials have crystallographically equivalent Na sites, and diffusion of Na^+ occurs from one side to the other. In O-type phases, there is only one occupancy site for Na-ions. In the case of Na^+ conduction in O3 type LOs, the diffusion of Na-ions from one octahedral site to the other involves Na^+ jumping to a metastable tetrahedral site first, this causes the formation of a high

activation barrier due to the difference in geometry [14, 15]. Additionally, strong coulombic repulsions between Na^+ ions in the tetrahedral sites and the metal ions in the TMO_2 layers raise the energy of the barrier even further. The diffusion mechanisms of P2 and O3 types are depicted in Fig. 1.8.

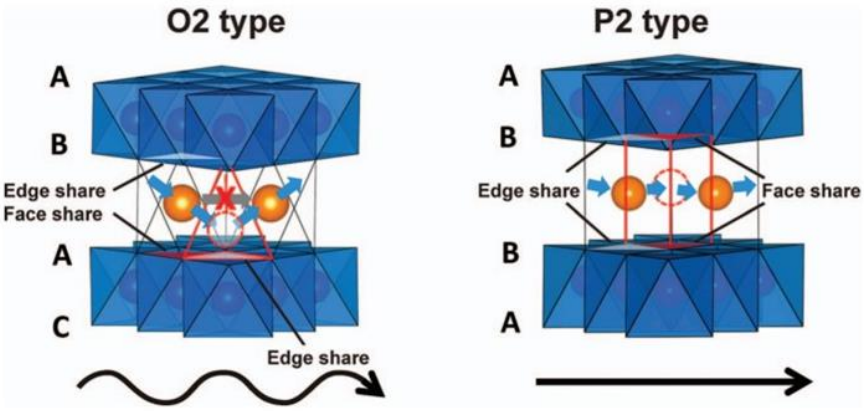

Figure 1.8. Pathway for Na^+ migration in O2 and P2 type LOs.

1.5. Literature Survey

Most of the P2-type LOs synthesized for research today consist of more than one TM element and are called polymetallic layered oxides (PLOs). PLOs are synthesized through cationic substitutions in monometallic layered oxides allowing researchers to tailor certain material properties by varying the TM layer compositions.

Among the combination of transition metals studied in P2-type materials, those based on Mn have received the most attention [8, 16]. Manganese is an earth-abundant resource, and P2-type Na_xMnO_2 cathodes have been reported to show high specific capacities close to 200 mAh/g. However, Mn-based cathodes suffer from low open circuit voltages (OCVs ~ 3 V) due to the low oxidation potential of the Mn^{3+}/Mn^{4+} redox couple (typically between 2 – 3 V). These cathodes also have poor cyclic performance due to detrimental distortions and phase transformations induced by Jahn-teller active Mn^{3+} ions at lower voltages [17, 18]. To circumvent this problem, Mn-based cathodes

have been doped with other TMs such as nickel and cobalt. Ni-ions exist predominantly in a 2+ oxidation state that forces Mn-ions to maintain a 4+ state which is Jahn teller inactive, during charging/discharging. Ni^{2+}–Ni^{4+} involves a 2-electron transfer instead of the one-electron transfer of the Mn^{3+}/Mn^{4+} redox couple, which makes up for the reduction in specific capacity from the loss of active Mn^{3+}/Mn^{4+} redox couples [19, 20]. This was demonstrated by Quannian et al. [21] and Manikandan et al. [22] where Mn was substituted with Ni. The former group prepared a P2-type $Na_{2/3}Ni_{1/3}Mn_{2/3}O_2$ and reported an initial capacity of 93 mAh/g with 90% capacity retained after 100 cycles at 0.1C when cycled between 2-4.2 V. In comparison, the latter group reported an impressive capacity of 167 mAh/g for the P2-type $Na_{2/3}Ni_{1/3}Mn_{2/3}O_2$ cathode when cycled at 0.1C between 1.5-4.5V with 80% capacity retained after 50 cycles. In the case of cobalt substitution for manganese, a specific capacity of 125 mAh/g was reported at a 0.1C rate for $NaCo_{0.5}Mn_{0.5}O_2$ by Yang et al. [23]. The material was also found to have excellent rate capabilities as it was able to show a capacity of 85 mAh/g even at a 5C rate. In a recent study, Li et al. prepared $Na_{0.7}Ni_{0.2}Co_{0.1}Mn_{0.7}O_2$ [24], where it was reported that Ni/Co co-doping had improved the structural stability and electrical conductivity of the cathode leading to a specific capacity of 155 mAh/g at 0.1C with 95% capacity retention after 92% capacity retained at 1C. Similar findings were also reported by Yuan et al. [25], where a capacity of 141 mAh/g was reported for $Na_{0.7}Ni_{0.15}Co_{0.20}Mn_{0.7}O_2$ cathode with 87 % capacity retention after 50 cycles at 0.1C discharge rate between 2-4.25V.

To circumvent the problem of phase transition at higher voltages in Ni and Co substituted, Yang et al. prepared $Na_{0.67}Ni_{0.18}Cu_{0.15}Mn_{0.67}O_2$ [26], which led to a substantial improvement in cyclic properties. The material was reported to have an initial capacity of 115 mAh/g at 0.1C, with 83% of capacity retained after 1000 cycles. Cu^{2+} substitution was found to stabilize the P2 structure at higher voltages, improving the cyclic performance and material stability in the ambient environment.

The investigations by Wang et al. [27] and Ma et al. [28] into Cu/Ni co-doped cathodes yielded similar results where Cu^{2+} substituted cathodes showed significant improvements in cyclic performance compared to the undoped cathode sample. Co substituted samples also showed better performance at higher voltages and phase transition was observed to shift from 4 V to 4.3 V [29]. In Ni and Co co-doped samples, Chen et al. [30] obtained a capacity of 131 mAh/g in $Na_{0.67}Ni_{0.2}Co_{0.1}Cu_{0.1}$ $Mn_{0.6}O_2$ cathode. Even at a high discharge rate of 8C, a capacity of 85 mAh/g was obtained, with 80% capacity retained after 500 cycles.

Fe has recently been extensively explored as a substituent, mainly because it is cheaper and is readily available. Fe was found to cause oxygen vacancies in lithium-based LOs due to the high redox potential of the $Fe^{3+/4+}$ couple, but in Na-based materials, Fe is relatively stable and electrochemically active [13]. A high concentration of Fe is not preferred in LOs due to its tendency to migrate from its original position resulting in capacity losses. The electrochemical properties of P2 type $Na_{2/3}Fe_{1/3}Mn_{2/3}O_2$ were studied by Zhao et al. [31]. At 4.3 V, a high concentration of unstable high spin Fe^{4+} ions was found, which induced a phase change from P2 to OP4. This phase was only partially reversible and was reported as the leading cause of capacity fading in Fe-based materials during cycling. Overall, $Na_{2/3}Fe_{1/3}Mn_{2/3}O_2$ cathode delivered a discharge capacity of 191 mAh/g at a 1/20 C rate with 80% charge retention after 40 cycles. To stabilize the structure of Fe-based cathodes, Yang et al. [19] synthesised P2-type $Na_{7/9}Cu_{2/9}Fe_{1/9}Mn_{2/3}O_2$. During cycling, Cu^{2+}/Cu^{3+} redox couples contributed to most of the capacity, while a small quantity of transfer of Mn^{3+} to Mn^{4+} and Fe^{3+} to Fe^{4+} was also detected. The compound showed no phase transitions during cycling even at 4.2 V and a discharge capacity of 89 mAh/g and 64 mAh/g at 0.1C and 1C rates, respectively, with 87% of the initial discharge retained after 150 cycles at 1C rate. Co-doping of Fe with Ni and Co was found to improve the average potential of the cathode with rapid degradation in the cyclic performance [32].

Recently, the doping of electrochemically inactive elements in the TM layers has been explored to further enhance rate performance and cycle life. Elements such as zinc [33, 34], magnesium [12, 35], aluminium [36, 37], and titanium have been used as pillar ions to support & stabilise the structure during the extraction of Na-ions. The presence of these elements has also been observed to help in the suppression of Na-ion vacancy ordering during charging. Vacancy ordering of Na-ions in layered oxides hinders Na-ion diffusion and induces phase transformations during the cycling [38-40]. Zn and Mg ions exist in a 2+ oxidation state and push other TM elements to a higher oxidation state which can cause a dip in a specific capacity. In contrast, Ti-ions [41] maintain a 4+ oxidation state and can, therefore, be used to play the same role as Mn^{4+} ions in the material without any significant loss in capacity.

In Fe-based compounds, Gonzalo et al. have reported an impressive capacity of 155 mAh/g in $Na_{2/3}Mn_{0.8}Fe_{0.1}Ti_{0.1}O_2$ [42] cathode with an 89% capacity retained after 300 cycles at 1C compared to 50% capacity retention of the unsubstituted cathode at 0.1C. In the case of Ni and Co-based compounds, Ti^{4+} ions have been reported to stabilise the P2 structure at high voltages by forming pillars for TMO_6 slabs, reducing volume shrinkages during cycling. Their inclusion into the structural framework also allows the enlargement of the NaO_2 layers with the contraction of the TMO_6 octahedron allowing better conduction of Na-ions, resulting in improved rate performance [43-45].

1.6. Motivation

About 80% of the energy generated in India comes from non-renewable energy sources. As pollution and climate change become more prominent, the race to better exploit renewable energy sources is gaining momentum. Currently, renewable energy sources generate only about 110 TWh of energy in India [46]. Figure 1.9 shows the contribution of each source toward energy production in India.

With the target of achieving 'Net Zero Emissions' by 2060, this share of renewable energy production is expected to increase exponentially in the coming decade. Most renewable energy sources do not provide a constant output and need an energy storage system to store energy in times of surplus to compensate in times of deficiency. As the renewable energy sector grows, so does the demand for stationary storage systems (Fig. 1.10). Batteries based on Li-ions are not expected to be able to meet the demand owing to lithium scarcity and the issues related to Li recycling.

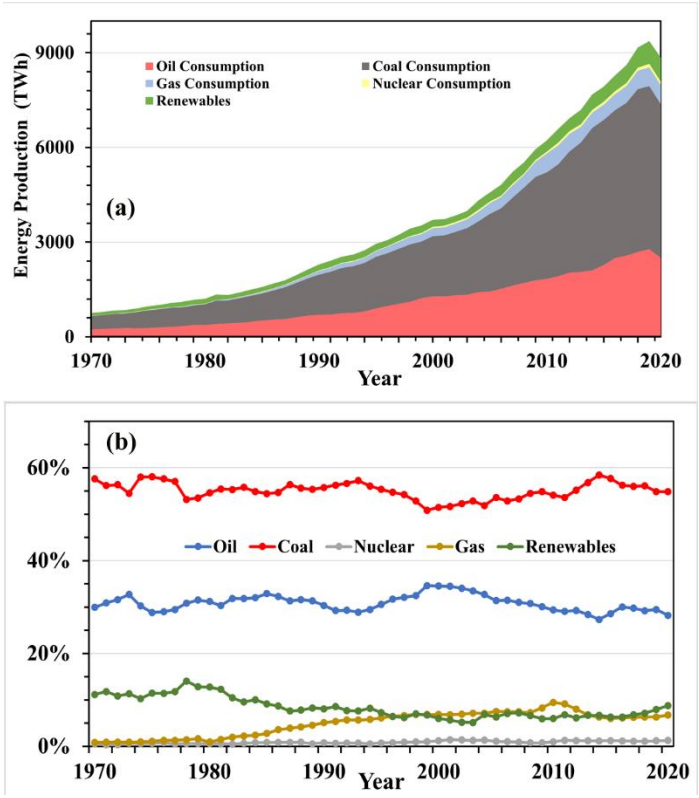

Figure 1.9. (a) Energy production by source, (b) percentage share of energy production by source in India.

Na-ion batteries are widely regarded as a possible alternative to replace LIBs to meet future needs, especially in stationary storage applications [47]. Cathodes being the primary source of Na-ions in a battery predominantly determines its overall performance. $Na_{0.70}Ni_{0.20}Cu_{0.15}Mn_{0.65}O_2$ is a P2 type layered oxide cathode based on Ni and Cu, which has been reported to exhibit a high capacity of 90 mAh/g

with more than 80 % of capacity retained after 1000 cycles at C/10 rate.

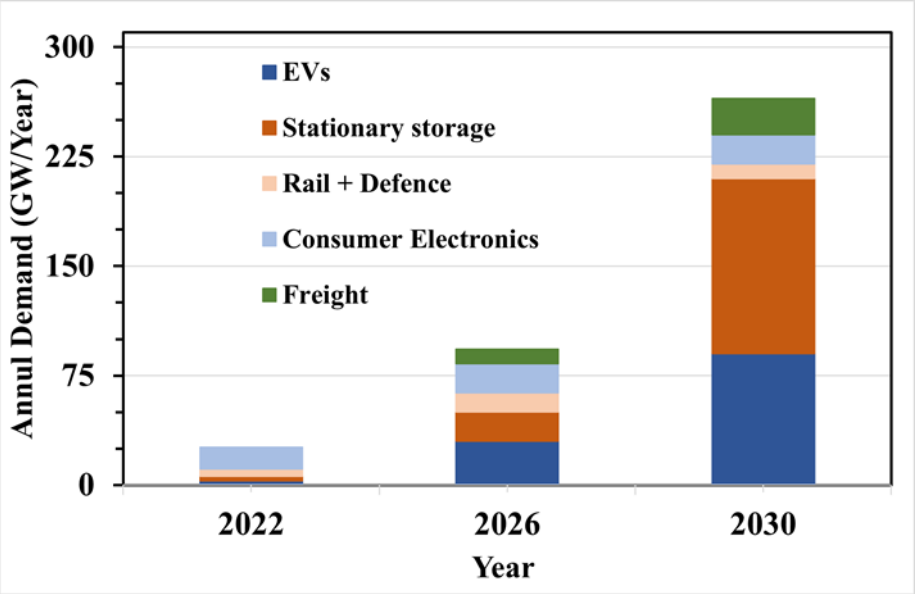

Figure 1.10. The expected growth rate of batteries based on their application in India.

In this thesis, Mn^{4+} in $Na_{0.70}Ni_{0.20}Cu_{0.15}Mn_{0.65}O_2$ was substituted with Ti^{4+} to refine further the $Na_x(Ni–Cu–Mn)O_2$ system to achieve better capacity and rate performance. Ti^{4+} ions, being electrochemically inactive, have been reported to stabilise the P2 structure at high voltages by forming pillars for TMO_6 slabs, reducing volume shrinkages during cycling, and improving cyclability and rate performance.

1.7. Objectives

This project aims to identify the optimum concentration of Ti doping in the $Na_{0.70}Cu_{0.15}Ni_{0.20}Mn_{0.65}O_2$ through an extensive study of the structural, electrical, and electrochemical characteristics. To achieve this, the following objectives are outlined.

1. To study the evolution of phase for the composition $Na_{0.70}Ni_{0.20}Cu_{0.15}Mn_{0.65}O_2$ as a function of calcination temperature.

2. To optimise the synthesis parameters for $Na_{0.70}Cu_{0.15}Ni_{0.20}Mn_{(0.65-x)}Ti_xO_2$ (NNCMT-*x*) materials

3. To understand the changes in the crystal structure, particle morphology, and uniform strain in NNCMT-*x* cathodes induced by Ti substitution.

4. Fabrication and electrochemical characterisation of cells using the prepared materials as the cathodes.

5. To explore the impact of Ti doping on the Na-ion diffusion coefficients, electrical conductivity, and electronic & ionic transference numbers to rationalise the observed electrochemical behaviour of NNCMT-*x* cathodes.

1.8. References

[1] K. Divya, J. Østergaard, Electric power systems research, 79 (2009) 511-520.

[2] P. Denholm, E. Ela, B. Kirby, M. Milligan, (2010).

[3] C. Vaalma, D. Buchholz, M. Weil, S. Passerini, Nature Reviews Materials, 3 (2018) 18013.

[4] R. Usiskin, Y. Lu, J. Popovic, M. Law, P. Balaya, Y.-S. Hu, J. Maier, Nature Reviews Materials, 6 (2021) 1020-1035.

[5] L. Qiao, X. Judez, T. Rojo, M. Armand, H. Zhang, Journal of The Electrochemical Society, 167 (2020) 070534.

[6] V. Palomares, P. Serras, I. Villaluenga, K.B. Hueso, J. Carretero-González, T. Rojo, Energy & Environmental Science, 5 (2012) 5884-5901.

[7] J.-Y. Hwang, S.-T. Myung, Y.-K. Sun, Chemical Society Reviews, 46 (2017) 3529-3614.

[8] R.J. Clément, P.G. Bruce, C.P. Grey, Journal of The Electrochemical Society, 162 (2015) A2589-A2604.

[9] C. Delmas, C. Fouassier, P. Hagenmuller, Physica B+C, 99 (1980) 81-85.

[10] N. Yabuuchi, K. Kubota, M. Dahbi, S. Komaba, Chemical Reviews, 114 (2014) 11636-11682.

[11] C. Zhao, Z. Yao, Q. Wang, H. Li, J. Wang, M. Liu, S. Ganapathy, Y. Lu, J. Cabana, B. Li, X. Bai, A. Aspuru-Guzik, M. Wagemaker, L. Chen, Y.-S. Hu, Journal of the American Chemical Society, 142 (2020) 5742-5750.

[12] P.-F. Wang, Y. You, Y.-X. Yin, Y.-S. Wang, L.-J. Wan, L. Gu, Y.-G. Guo, Angewandte Chemie International Edition, 55 (2016) 7445-7449.

[13] N. Yabuuchi, M. Kajiyama, J. Iwatate, H. Nishikawa, S. Hitomi, R. Okuyama, R. Usui, Y. Yamada, S. Komaba, Nature Materials, 11 (2012) 512-517.

[14] Z. Liu, X. Xu, S. Ji, L. Zeng, D. Zhang, J. Liu, Chemistry – A European Journal, 26 (2020) 7747-7766.

[15] L.A. Ma, R. Palm, E. Nocerino, O.K. Forslund, N. Matsubara, S. Cottrell, K. Yokoyama, A. Koda, J. Sugiyama, Y. Sassa, M. Månsson, R. Younesi, Physical Chemistry Chemical Physics, 23 (2021) 24478-24486.

[16] J. Darga, J. Lamb, A. Manthiram, Energy Technology, 8 (2020) 2000723.

[17] D. Kundu, E. Talaie, V. Duffort, L.F. Nazar, Angewandte Chemie International Edition, 54 (2015) 3431-3448.

[18] J. Billaud, R.J. Clément, A.R. Armstrong, J. Canales-Vázquez, P. Rozier, C.P. Grey, P.G. Bruce, Journal of the American Chemical Society, 136 (2014) 17243-17248.

[19] Y. Li, Z. Yang, S. Xu, L. Mu, L. Gu, Y.-S. Hu, H. Li, L. Chen, Adv Sci (Weinh), 2 (2015) 1500031-1500031.

[20] Y. Zhang, R. Zhang, Y. Huang, Frontiers in Chemistry, 7 (2019).

[21] Q. Liu, Z. Hu, M. Chen, C. Zou, H. Jin, S. Wang, Q. Gu, S. Chou, Journal of Materials Chemistry A, 7 (2019) 9215-9221.

[22] P. Manikandan, D. Ramasubramonian, M.M. Shaijumon, Electrochimica Acta, 206 (2016) 199-206.

[23] P. Yang, C. Zhang, M. Li, X. Yang, C. Wang, X. Bie, Y. Wei, G. Chen, F. Du, Chemphyschem, 16 (2015) 3408-3412.

[24] Z.-Y. Li, R. Gao, L. Sun, Z. Hu, X. Liu, Journal of Materials Chemistry A, 3 (2015) 16272-16278.

[25] D. Yuan, W. He, F. Pei, F. Wu, Y. Wu, J. Qian, Y. Cao, X. Ai, H. Yang, Journal of Materials Chemistry A, 1 (2013) 3895-3899.

[26] L. Yang, S.-h. Luo, Y. Wang, Y. Zhan, Q. Wang, Y. Zhang, X. Liu, W. Mu, F. Teng, Chemical Engineering Journal, 404 (2020) 126578.

[27] L. Wang, Y.-G. Sun, L.-L. Hu, J.-Y. Piao, J. Guo, A. Manthiram, J. Ma, A.-M. Cao, Journal of Materials Chemistry A, 5 (2017) 8752-8761.

[28] P. Ma, W. Kang, Y. Wang, D. Cao, L. Fan, D. Sun, Applied Surface Science, 529 (2020) 147105.

[29] W.-L. Pang, J.-Z. Guo, X.-H. Zhang, C.-Y. Fan, X.-J. Nie, H.-Y. Yu, W.-H. Li, Q. Yang, X.-L. Wu, Journal of Alloys and Compounds, 790 (2019) 1092-1100.
[30] T. Chen, W. Liu, Y. Zhuo, H. Hu, M. Zhu, R. Cai, X. Chen, J. Yan, K. Liu, Journal of Energy Chemistry, 43 (2020) 148-154.
[31] J. Zhao, J. Xu, D.H. Lee, N. Dimov, Y.S. Meng, S. Okada, Journal of Power Sources, 264 (2014) 235-239.
[32] S. Chu, Y. Chen, J. Wang, J. Dai, K. Liao, W. Zhou, Z. Shao, Journal of Alloys and Compounds, 775 (2019) 383-392.
[33] X. Wu, G.-L. Xu, G. Zhong, Z. Gong, M.J. McDonald, S. Zheng, R. Fu, Z. Chen, K. Amine, Y. Yang, ACS Applied Materials & Interfaces, 8 (2016) 22227-22237.
[34] X. Wu, J. Guo, D. Wang, G. Zhong, M.J. McDonald, Y. Yang, Journal of Power Sources, 281 (2015) 18-26.
[35] Y. Chen, G. Su, X. Cheng, T. Du, Y. Han, W. Qiang, B. Huang, Journal of Alloys and Compounds, 858 (2021) 157717.
[36] E. Marelli, C. Villevieille, S. Park, N. Hérault, C. Marino, ACS Applied Energy Materials, 1 (2018) 5960-5967.
[37] S. Altin, S. Altundağ, E. Altin, M. Harfouche, A. Bayri, Journal of Materials Science: Materials in Electronics, 31 (2020) 14784-14794.
[38] A.J. Toumar, S.P. Ong, W.D. Richards, S. Dacek, G. Ceder, Physical Review Applied, 4 (2015) 064002.
[39] A. Gutierrez, W.M. Dose, O. Borkiewicz, F. Guo, M. Avdeev, S. Kim, T.T. Fister, Y. Ren, J. Bareño, C.S. Johnson, The Journal of Physical Chemistry C, 122 (2018) 23251-23260.
[40] P.-F. Wang, H.-R. Yao, X.-Y. Liu, Y.-X. Yin, J.-N. Zhang, Y. Wen, X. Yu, L. Gu, Y.-G. Guo, Science Advances, 4 (2018) eaar6018.
[41] T. Lan, W. Wei, S. Xiao, G. He, J. Hong, Journal of Materials Science: Materials in Electronics, 31 (2020) 9423-9429.
[42] J.-k. Park, G.-g. Park, H.H. Kwak, S.-T. Hong, J.-w. Lee, ACS Omega, 3 (2018) 361-368.

[43] H. Yoshida, N. Yabuuchi, K. Kubota, I. Ikeuchi, A. Garsuch, M. Schulz-Dobrick, S. Komaba, Chemical Communications, 50 (2014) 3677-3680.

[44] S. Tao, W. Zhou, D. Wu, Z. Wang, B. Qian, W. Chu, A. Marcelli, L. Song, Journal of Materials Science & Technology, 74 (2021) 230-236.

[45] Q.-C. Wang, E. Hu, Y. Pan, N. Xiao, F. Hong, Z.-W. Fu, X.-J. Wu, S.-M. Bak, X.-Q. Yang, Y.-N. Zhou, Advanced Science, 4 (2017) 1700219.

[46] E. Panos, M. Densing, K. Volkart, Energy Strategy Reviews, 9 (2016) 28-49.

[47] R. NITI Aayog, and RMI India, in, India, 2022.

MATERIALS and METHODS

2.1. Sol-Gel Synthesis

The P2-type $Na_{0.70}Ni_{0.20}Cu_{0.15}Mn_{(0.65-x)}Ti_xO_2$ (x = 0, 0.025, 0.050, 0.075, and 0.100) materials were synthesised using a simple sol-gel method. Sol-gel synthesis is ideal for the homogeneous mixing of precursors. Stoichiometric amounts of nickel acetate tetrahydrate, copper (II) nitrate trihydrate, manganese (II) acetate tetrahydrate, titanium (IV) bis(ammonium lactato)dihydroxide (50 wt% aq.), and sodium carbonate (10% excess sodium to compensate for losses during calcination) were dissolved in DI water and stirred for 6 h after which appropriate amounts of ethylene glycol and citric acid were added.

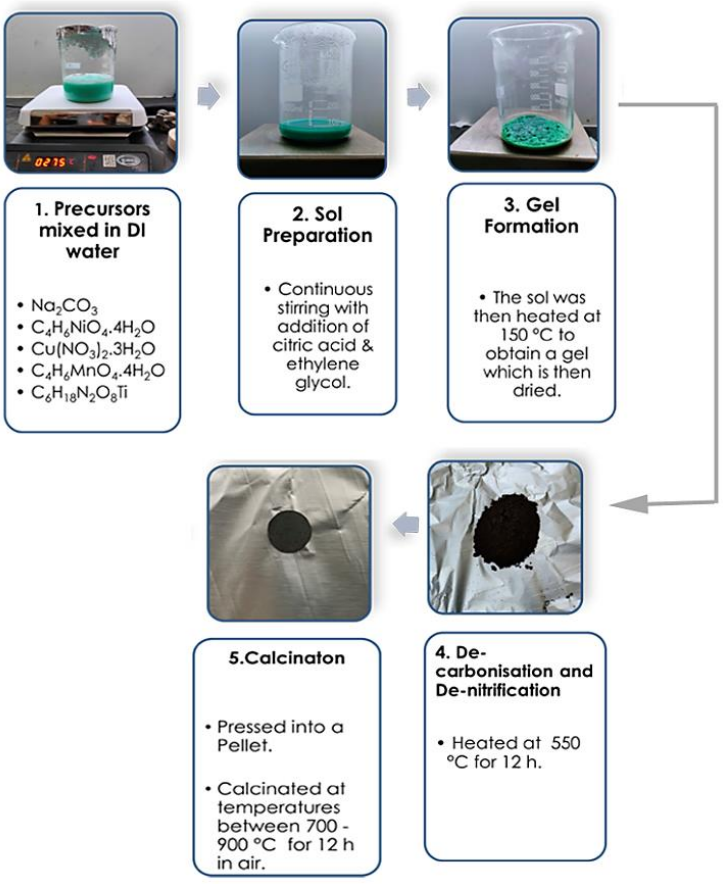

Figure 2.1. The steps involved in Sol-gel synthesis.

The resulting solution was continuously stirred for 12 h and then heated at ~ 80 °C to obtain a gel. The gel was dried, ground, and heat-treated at 550 °C in air for 12 h. The resulting powder was ground

again and calcinated at different temperatures (700 – 1000 ℃) for 12 h in air to obtain the final product. Figure 2.1 shows a schematic of the processes involved in the sol-gel method.

2.2. Fabrication

2.2.1. Ceramic Fabrication

For impedance measurements, some amount of the powder for each of the samples, after being heated at 550 ℃ for 12 h, was ground using mortar and pestle, pressed into a pellet and sintered at 1000 ℃ for 6 h in air. Sintering is a type of heat treatment process involved in ceramic fabrication where grains grow due to diffusion, reduce porosity, and densify the ceramic.

Figure 2.2. The apparatus used in ceramic fabrication.

Optimum sintering temperature and duration vary with ceramic type and is below its melting point. All the pellets sintered for impedance measurements were ~ 90% dense. The equipment used in the ceramic fabrication are shown in Fig. 2.2.

2.2.2. Cathode Preparation

Electrochemical studies were conducted on a coin cell with the active material as the cathode. The cathode was prepared by mixing 85 wt.% active material, 5 wt.% Ketjen black, and 10 wt.% C arboxymethyl cellulose (CMC) binder in DI water. Ketjen black is added to improve the electronic conductivity of the cathode layer, while CMC is the binder that allows the slurry to stick onto the current collector. The slurry was then coated on an Al current collector using a desktop coater and doctor blade (Fig. 2.3) and dried at 100 °C for 12 h in a vacuum oven. Circular cathode discs of 16 mm diameter were then punched from the dried sheet to be used as the cathode in coin cells

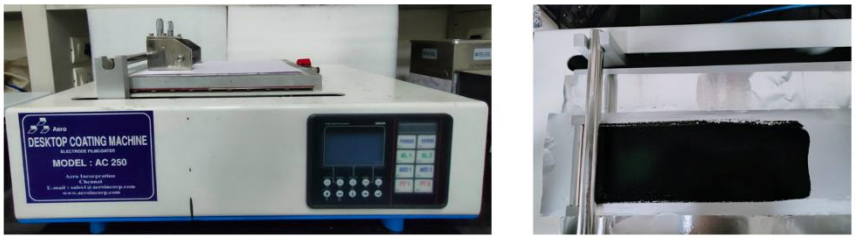

Figure 2.3. Desktop film coater used in cathode preparation.

2.2.3 Coin Cell Assembly

CR-2032 coin cells were fabricated using the circular cathode discs and Na metal as the counter electrode in an Argon filled glove box. Celgard 2400 was used as the separator with 1M $NaBF_4$ dissolved in tetraethylene glycol dimethyl ether (tetraglyme) acting as the electrolyte. The inert atmosphere of argon is required to prevent the contamination of Na metal and electrolyte . Figure 2.4 shows all the components and their order arrangement inside a coin cell.

Figure 2.4. Various components of a coin cell

2.3. Structural Characterization

2.3.1. X-ray Diffraction

The room temperature crystal structures of the samples were characterized using powder x-ray diffraction (XRD) by employing an Empyrean, Malvern Pananalytical diffractometer (Fig. 2.5), with Cu-Kα radiation source in the 2θ range of 10° – 80° and the crystallographic parameters of all samples were estimated from the Rietveld refinement of the XRD data using the software package *TOPAS Academic* (version 6) [48]. XRD analysis is a versatile and non-destructive characterization technique used for phase confirmation, identifying lattice parameters, phase purity, lattice strain, etc.

Figure 2.5. The Malvern Pananalytical diffractometer.

2.3.2. Field Emission Scanning Electron Microscopy (FESEM)

FESEM is a high-resolution imaging technique used to study surface morphology, particle size, and shape. A field emission scanning electron microscope (model JEOL-7610) equipped with energy-dispersive x-ray spectroscopy (EDS) was used to study the morphology and distribution of constituent elements of powder samples (Fig. 2.6).

2.3.3. X-ray Photoelectron Spectroscopy

X-ray photoelectron spectroscopy (XPS) was performed to verify the oxidation states of constituent transition metals in the samples. XPS identifies the oxidation states of various elements by analyzing the energy of the photoelectrons generated by X-rays beamed from the instrument. XPS measurements were taken using Thermofisher Scientific (Naxsa base) with an Al Kα X-ray source (1486.6 eV).

Figure 2.6. The JEOL-7610 Field Emission Scanning Electron Microscope.

2.4. Electrical Characterisation

2.4.1. Complex Impedance Spectroscopy

For impedance studies, the sintered pellets were polished flat, electroded with silver paste on either side, and cured at 650 °C for 10 min after drying. Impedance measurements were done on the pellets using a computer-controlled LCR meter (model: ZM 2376, NF Corp.) by applying a 50 mV ac signal in the 1 Hz – 1 MHz frequency range (Fig. 2.7). Complex impedance spectroscopy is a versatile technique used to characterize a variety of materials in terms of their electrical behaviour by measuring the impedance over a wide range of frequencies, typically ranging from 10^{-2} to 10^{7} Hz. This helps map the sample based on their electrical conduction and identify the dominant resistive component in the sample.

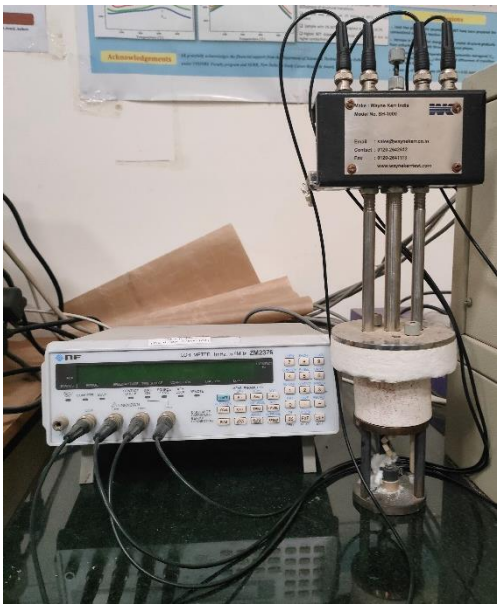

Figure 2.7. The LCR meter (left) and the sample holder (right).

2.4.2. Chronoamperometry

The contribution of the dominant conducting species towards overall conduction can be ascertained through chronoamperometry which isolates electronic conduction from ionic conduction. Chronoamperometry was performed to estimate the Na^+ transference number ($t_{Na)}$ using the Keithley Source Meter Unit (model 2450-EC) under an applied voltage of 1 V.

2.5. Electrochemical Characterization

2.5.1. Cyclic Voltammetry

To investigate the redox process in the prepared cathode materials, cyclic voltammetry (CV) was performed on the coin cells between a potential window of 2.00 - 4.25 V with a scan rate of 0.1 mV/s using the Keithley source meter unit (Model 2450-EC). CV curves are voltage vs. current plots that are used to identify redox couples responsible for charge compensation during the extraction and insertion of Na ions in different electrodes.

2.5.2. Galvanostatic Charge/Discharge

Galvanometric charge-discharge tests were carried out using a Landt battery testing system (LANHE CT 2001A, shown in Fig. 2.8). The rate performance tests were performed at 0.1C, 0.2C, 0.3C, 0.5C, 1C, 2C, and 3C, while the cyclic performance was evaluated at 1C for 300 cycles between 2.00 V to 4.25 V. The mass loading for each of the samples was adjusted to ~ 2 mg/cm^{2,} and all C-rates were taken based on the specific capacity of 125 mAh/g.

Figure 2.8 The LANHE battery tester.

2.6. References

[1] K. Divya, J. Østergaard, Electric power systems research, 79 (2009) 511-520.

[2] P. Denholm, E. Ela, B. Kirby, M. Milligan, (2010).

[3] C. Vaalma, D. Buchholz, M. Weil, S. Passerini, Nature Reviews Materials, 3 (2018) 18013.

[4] R. Usiskin, Y. Lu, J. Popovic, M. Law, P. Balaya, Y.-S. Hu, J. Maier, Nature Reviews Materials, 6 (2021) 1020-1035.

[5] L. Qiao, X. Judez, T. Rojo, M. Armand, H. Zhang, Journal of The Electrochemical Society, 167 (2020) 070534.

[6] V. Palomares, P. Serras, I. Villaluenga, K.B. Hueso, J. Carretero-González, T. Rojo, Energy & Environmental Science, 5 (2012) 5884-5901.

[7] J.-Y. Hwang, S.-T. Myung, Y.-K. Sun, Chemical Society Reviews, 46 (2017) 3529-3614.

[8] R.J. Clément, P.G. Bruce, C.P. Grey, Journal of The Electrochemical Society, 162 (2015) A2589-A2604.

[9] C. Delmas, C. Fouassier, P. Hagenmuller, Physica B+C, 99 (1980) 81-85.

[10] N. Yabuuchi, K. Kubota, M. Dahbi, S. Komaba, Chemical Reviews, 114 (2014) 11636-11682.

[11] C. Zhao, Z. Yao, Q. Wang, H. Li, J. Wang, M. Liu, S. Ganapathy, Y. Lu, J. Cabana, B. Li, X. Bai, A. Aspuru-Guzik, M. Wagemaker, L. Chen, Y.-S. Hu, Journal of the American Chemical Society, 142 (2020) 5742-5750.

[12] P.-F. Wang, Y. You, Y.-X. Yin, Y.-S. Wang, L.-J. Wan, L. Gu, Y.-G. Guo, Angewandte Chemie International Edition, 55 (2016) 7445-7449.

[13] N. Yabuuchi, M. Kajiyama, J. Iwatate, H. Nishikawa, S. Hitomi, R. Okuyama, R. Usui, Y. Yamada, S. Komaba, Nature Materials, 11 (2012) 512-517.

[14] Z. Liu, X. Xu, S. Ji, L. Zeng, D. Zhang, J. Liu, Chemistry – A European Journal, 26 (2020) 7747-7766.

[15] L.A. Ma, R. Palm, E. Nocerino, O.K. Forslund, N. Matsubara, S. Cottrell, K. Yokoyama, A. Koda, J. Sugiyama, Y. Sassa, M. Månsson, R. Younesi, Physical Chemistry Chemical Physics, 23 (2021) 24478-24486.
[16] J. Darga, J. Lamb, A. Manthiram, Energy Technology, 8 (2020) 2000723.
[17] D. Kundu, E. Talaie, V. Duffort, L.F. Nazar, Angewandte Chemie International Edition, 54 (2015) 3431-3448.
[18] J. Billaud, R.J. Clément, A.R. Armstrong, J. Canales-Vázquez, P. Rozier, C.P. Grey, P.G. Bruce, Journal of the American Chemical Society, 136 (2014) 17243-17248.
[19] Y. Li, Z. Yang, S. Xu, L. Mu, L. Gu, Y.-S. Hu, H. Li, L. Chen, Adv Sci (Weinh), 2 (2015) 1500031-1500031.
[20] Y. Zhang, R. Zhang, Y. Huang, Frontiers in Chemistry, 7 (2019).
[21] Q. Liu, Z. Hu, M. Chen, C. Zou, H. Jin, S. Wang, Q. Gu, S. Chou, Journal of Materials Chemistry A, 7 (2019) 9215-9221.
[22] P. Manikandan, D. Ramasubramonian, M.M. Shaijumon, Electrochimica Acta, 206 (2016) 199-206.
[23] P. Yang, C. Zhang, M. Li, X. Yang, C. Wang, X. Bie, Y. Wei, G. Chen, F. Du, Chemphyschem, 16 (2015) 3408-3412.
[24] Z.-Y. Li, R. Gao, L. Sun, Z. Hu, X. Liu, Journal of Materials Chemistry A, 3 (2015) 16272-16278.
[25] D. Yuan, W. He, F. Pei, F. Wu, Y. Wu, J. Qian, Y. Cao, X. Ai, H. Yang, Journal of Materials Chemistry A, 1 (2013) 3895-3899.
[26] L. Yang, S.-h. Luo, Y. Wang, Y. Zhan, Q. Wang, Y. Zhang, X. Liu, W. Mu, F. Teng, Chemical Engineering Journal, 404 (2020) 126578.
[27] L. Wang, Y.-G. Sun, L.-L. Hu, J.-Y. Piao, J. Guo, A. Manthiram, J. Ma, A.-M. Cao, Journal of Materials Chemistry A, 5 (2017) 8752-8761.
[28] P. Ma, W. Kang, Y. Wang, D. Cao, L. Fan, D. Sun, Applied Surface Science, 529 (2020) 147105.

[29] W.-L. Pang, J.-Z. Guo, X.-H. Zhang, C.-Y. Fan, X.-J. Nie, H.-Y. Yu, W.-H. Li, Q. Yang, X.-L. Wu, Journal of Alloys and Compounds, 790 (2019) 1092-1100.
[30] T. Chen, W. Liu, Y. Zhuo, H. Hu, M. Zhu, R. Cai, X. Chen, J. Yan, K. Liu, Journal of Energy Chemistry, 43 (2020) 148-154.
[31] J. Zhao, J. Xu, D.H. Lee, N. Dimov, Y.S. Meng, S. Okada, Journal of Power Sources, 264 (2014) 235-239.
[32] S. Chu, Y. Chen, J. Wang, J. Dai, K. Liao, W. Zhou, Z. Shao, Journal of Alloys and Compounds, 775 (2019) 383-392.
[33] X. Wu, G.-L. Xu, G. Zhong, Z. Gong, M.J. McDonald, S. Zheng, R. Fu, Z. Chen, K. Amine, Y. Yang, ACS Applied Materials & Interfaces, 8 (2016) 22227-22237.
[34] X. Wu, J. Guo, D. Wang, G. Zhong, M.J. McDonald, Y. Yang, Journal of Power Sources, 281 (2015) 18-26.
[35] Y. Chen, G. Su, X. Cheng, T. Du, Y. Han, W. Qiang, B. Huang, Journal of Alloys and Compounds, 858 (2021) 157717.
[36] E. Marelli, C. Villevieille, S. Park, N. Hérault, C. Marino, ACS Applied Energy Materials, 1 (2018) 5960-5967.
[37] S. Altin, S. Altundağ, E. Altin, M. Harfouche, A. Bayri, Journal of Materials Science: Materials in Electronics, 31 (2020) 14784-14794.
[38] A.J. Toumar, S.P. Ong, W.D. Richards, S. Dacek, G. Ceder, Physical Review Applied, 4 (2015) 064002.
[39] A. Gutierrez, W.M. Dose, O. Borkiewicz, F. Guo, M. Avdeev, S. Kim, T.T. Fister, Y. Ren, J. Bareño, C.S. Johnson, The Journal of Physical Chemistry C, 122 (2018) 23251-23260.
[40] P.-F. Wang, H.-R. Yao, X.-Y. Liu, Y.-X. Yin, J.-N. Zhang, Y. Wen, X. Yu, L. Gu, Y.-G. Guo, Science Advances, 4 (2018) eaar6018.
[41] T. Lan, W. Wei, S. Xiao, G. He, J. Hong, Journal of Materials Science: Materials in Electronics, 31 (2020) 9423-9429.
[42] J.-k. Park, G.-g. Park, H.H. Kwak, S.-T. Hong, J.-w. Lee, ACS Omega, 3 (2018) 361-368.
[43] H. Yoshida, N. Yabuuchi, K. Kubota, I. Ikeuchi, A. Garsuch, M. Schulz-Dobrick, S. Komaba, Chemical Communications, 50 (2014) 3677-3680.

[44] S. Tao, W. Zhou, D. Wu, Z. Wang, B. Qian, W. Chu, A. Marcelli, L. Song, Journal of Materials Science & Technology, 74 (2021) 230-236.
[45] Q.-C. Wang, E. Hu, Y. Pan, N. Xiao, F. Hong, Z.-W. Fu, X.-J. Wu, S.-M. Bak, X.-Q. Yang, Y.-N. Zhou, Advanced Science, 4 (2017) 1700219.
[46] E. Panos, M. Densing, K. Volkart, Energy Strategy Reviews, 9 (2016) 28-49.
[47] R. NITI Aayog, and RMI India, in, India, 2022.
[48] A. Coelho, Journal of Applied Crystallography, 51 (2018) 210-218.

Structural, Transport, and Electrochemical Properties of NNCM

This chapter deals with the structural, electrical, and electrochemical properties of P2-type $Na_{0.70}Ni_{0.20}Cu_{0.15}Mn_{0.65}O_2$ (NNCM) ceramic fabricated via a sol-gel method. The Rietveld refinement of the room temperature XRD diffraction data along with Field emission scanning electron microscopy was used to study investigate the structural characteristics of the powder calcined at 850 ℃. Complex impedance spectroscopy was used to deconvolute the contributions of grains and grain boundaries to the overall conduction inside the sample.

3.1. Structural properties

Figure 3.1 shows the phase evolution of NNCM with calcination temperature. P2 materials show their strongest peak at ~ 15.8°. The presence of this peak in the XRD pattern for the sample calcined at 550 ℃ indicates the presence of a P2 phase in the sample along with other peaks corresponding to unreacted precursors & intermediate phases. At higher calcination temperatures intensity of the peaks related to P2 is observed to increase while peaks corresponding to other impurity phases disappear. A single P2-type phase is obtained for the sample calcined at 850 ℃. Two minor peaks in the vicinity of $2\theta \approx 28°$ in the XRD pattern for this sample (denoted by *) suggest the ordering of Na^+ vacancies in $Na_{0.70}Ni_{0.20}Cu_{0.15}Mn_{0.65}O_2$ [1-3].

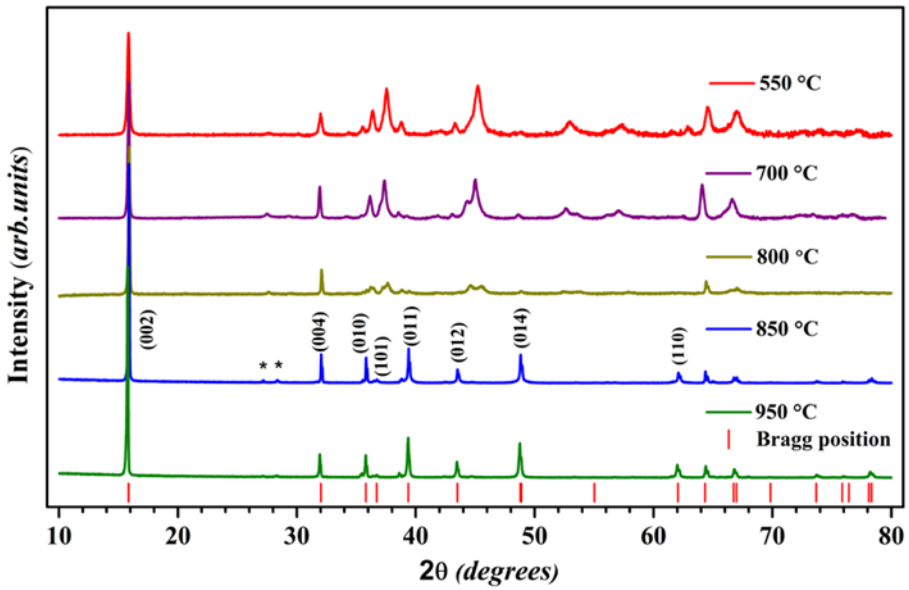

Figure 3.1. XRD patterns of NNCM samples calcined at different temperatures. The * symbol indicates peaks related to superlattice reflections caused by Na^+ vacancy ordering.

Rietveld refinement of the room temperature X-ray diffraction data for the sample sintered at 950 ℃ was carried out using the software package TOPAS Academic (version 6) [4]. The refinement profile, as shown in Fig. 3.2, confirms a single P2 phase based on a hexagonal symmetry with $P6_3/mmc$ space group for NNCM. A low-intensity peak observed at ~ 39° suggests the presence of minor CuO impurities. The fraction of this impurity was estimated to be less than 1% of the sample. The difference between the calculated and observed data is plotted as a dark grey line at the bottom in Fig. 3.2. The low intensity of the difference profile and small values of reliability factors (*GOF* = 1.77, R_{WP} = 19.2, R_P = 15.1, and R_{EXP} = 10.8) suggest the high accuracy of the refined crystal structure parameters and the choice of structure model.

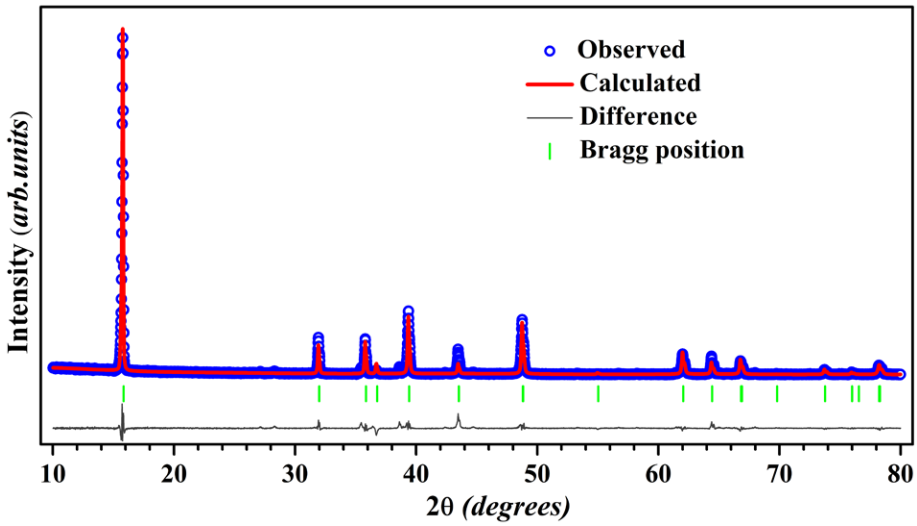

Figure 3.2. Rietveld refinement profile of room temperature XRD pattern of NNCM sample sintered at 1000 ºC for 12 h.

The lattice parameters for the hexagonal unit cell obtained after refinement were a = 2.8896 ± 0.0007 Å and c = 11.1803 ± 0.0005 Å. The cell volume V was calculated to be 81.850 ± 0.005 Å^3. These values concur with the data reported in the literature [5]. The crystallographic unit cell of the P2-type NNCM layered oxide based on the data from Rietveld refinement of the XRD data (see Table 3.1) is shown in Fig. 3.3.

Table. 3.1. Crystallographic parameters of P2-type NNMC obtained from Rietveld refinement of room temperature XRD data.

Atom	**x**	**y**	**z**	**Occupancy**	**Site**
Na1	2/3	1/3	1/4	0.45	2d
Na2	0	0	1/4	0.25	2b
Mn/Ni/ Cu	0	0	0	0.65/0.20/0.15	2a
O	2/3	1/3	0.089	1	4f

Software package VESTA was used to generate these images [6]. The volume of TM - O_6 octahedron for NNCM is calculated to be 9.678 Å^3, whereas the Na - O_6 prism volume is ~ 12.958Å^3. The area of the square bottleneck for the sodium intercalation at the Na-1 site (Fig. 3.3) is ~ 10.353 Å^2. Na-O and effective TM-O bond lengths are 2.448

± 0.005 Å and 1.947 ± 0.004 Å, respectively. The SEM image of the powder sample calcined at 850 °C is shown in Fig. 3.4(a). The powdered sample shows hexagonal plates with well-defined facets indicating good crystallinity (Fig. 3.4(a)). The particles were observed to have an average size of 1.9 μm ± 0.4 μm and an average thickness of about 0.25 μm. This corresponds to a typical aspect ratio of ~ 8. The (100), (010), (110), ($\bar{1}$00), (0$\bar{1}$0), ($\bar{1}\bar{1}$0) planes in NNCM hexagonal lattice have higher surface energies as compared {001} planes. Accordingly, the equilibrium shape of the NNCM crystal as predicted by Wulff plot is hexagon-type flakes with dominant {001} surfaces.

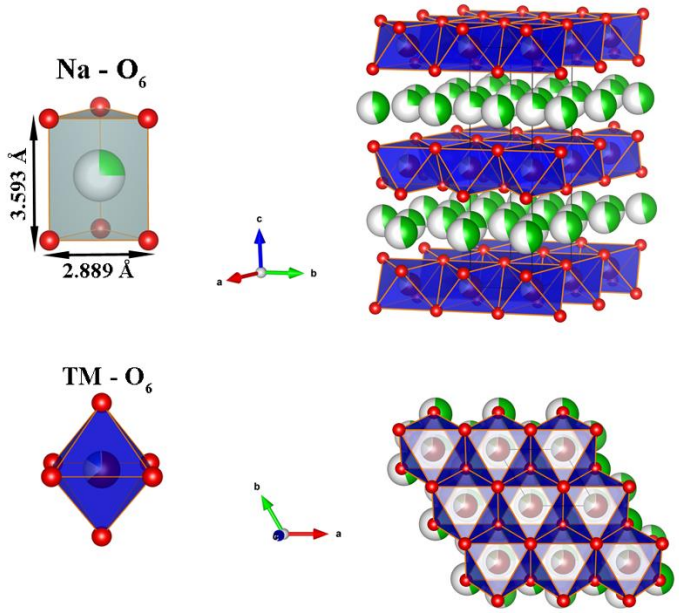

Figure. 3.3. Crystal structure of P2 type - NNCM sample visualized using VESTA.

The cross-sectional SEM image of a fractured surface of the pellet sintered at 1000 ℃ for 12 h (Fig. 3.4(b)) exhibits randomly oriented and tightly packed grains. The calculated relative density of the pellet was ~ 90 ± 2 %. Elemental mapping performed using EDS (shown in Fig. 3.4(c)) points to a uniform distribution of Na, Ni, Mn, Cu, and O elements throughout the sample. The segregation of Cu seen in Fig. 3.4(c1) is due to minor CuO impurities in the sample.

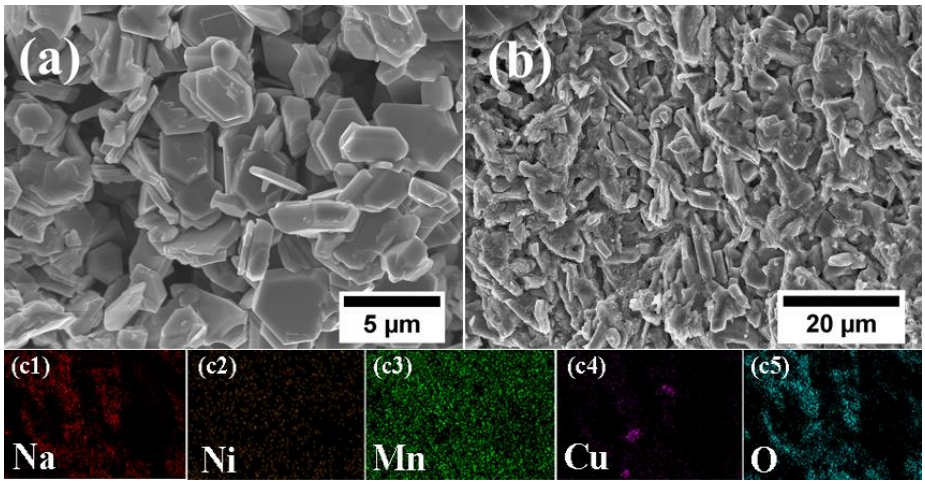

Figure 3.4. SEM image of NNCM (a) powder calcined at 850 °C (b) fractured surface of the pellet sintered at 950 °C (c) EDS maps of (c1) Na, (c2) Ni, (c3) Mn, (c4) Cu, and (c5) O for the sample surfaces shown in (b).

3.2. XPS Measurements

The oxidation states of the transition metals in NNCM were verified using X-ray photoelectron spectroscopy. The XPS spectra of Mn-2p, Ni-2p, Cu-2p, and Na-1s are displayed in Fig. 3.5. In the Mn-2p spectra, the peaks centred at 643 eV (Mn $2p_{3/2}$) and ~ 654 eV (Mn-$2p_{1/2}$) confirm the existence Mn^{4+} ions in the samples [7, 8]. The four characteristic peaks in the Ni-2p and Cu-2p spectra are attributed to Ni-$2p_{3/2}$ (~ 855 eV), Ni-$2p_{1/2}$ (~ 872 eV), Cu-$2p_{3/2}$ (~ 933 eV) and Cu-$2p_{1/2}$ (~ 953 eV) and their respective shake-up satellite peaks indicating that Ni and Cu maintained a +2 oxidation state in the sample [8, 9]. In the Na spectrum, the peak at ~ 1071 eV, indicating the +1 oxidation state of Na ions [8, 9], is quite broad and can be deconvoluted into 2

peaks pertaining to 2 different crystallographic sites for Na in the NNCM unit cell.

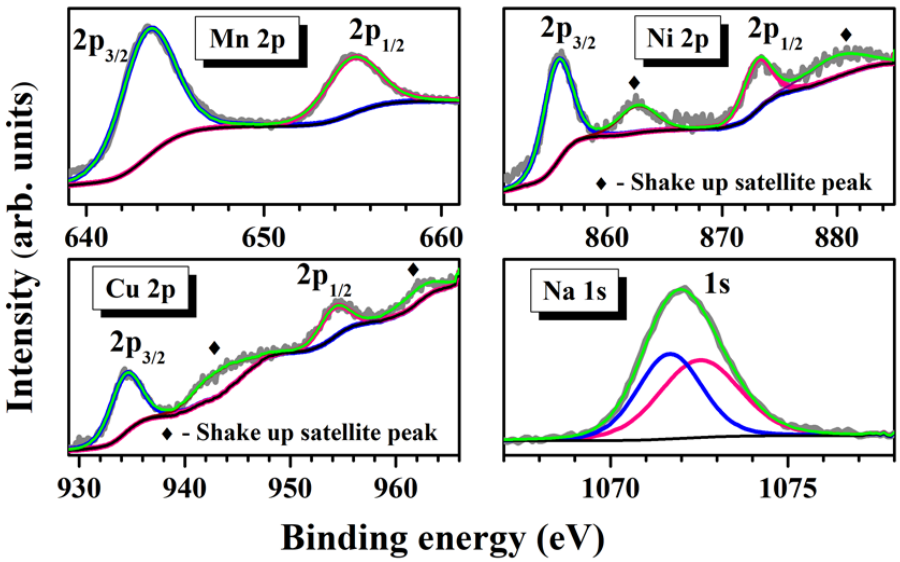

Figure 3.5. XPS spectra of as-prepared NNCM sample.

3.3. Electrical properties

To study the transport behaviour of NNCM, temperature-dependent impedance measurements were performed on the pelletised sample sintered at 1000 °C for 12 h. Nyquist plots (-Z″ versus Z′) plotted at various temperatures in the 300 – 325 K range are shown in Fig. 3.6. The plots show two semi-circular arcs at higher and intermediate frequencies, which are typically attributed to the contributions of grain and grain boundary towards overall impedance in the material. The third linear tail component seen at lower frequencies is due to sodium-ion blocking by the silver metal electrodes, suggesting substantial ionic conduction in NNCM. With the increase in temperature, the low-frequency intercepts of the semi-circular arc on the x-axis shift towards lower values (Figs. 3.6(a) & 3.6(b)). To deconvolute the contributions from grains, grain boundaries, and sample-electrode interface, the impedance is usually analyzed through equivalent circuit modeling.

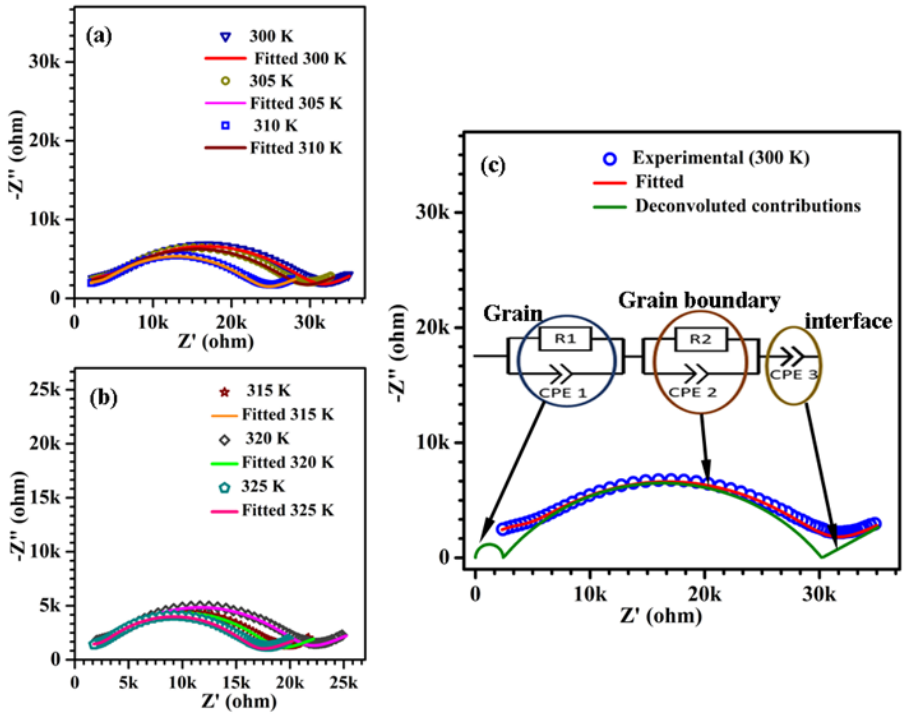

Figure 3.6. Nyquist plots of NNCM at different temperatures: (a) 300-310 K, (b) 315-325 K, and (c) 300 K. The impedance data were fitted using the equivalent circuit shown in Fig. 3.6(c) inset. The deconvoluted contributions of grain, grain boundary, and electrode interface to total impedance are depicted by the solid green line in Fig. 3.6(c).

Table. 3.2. Parameters obtained after fitting the impedance data of NNMC at 300 K.

Component	**Resistance (Ω)**	**C for CPE (F)**	***n* for CPE**
Grain	2425	1.00×10^{-10}	0.97
Grain Boundary	27790	9.96×10^{-8}	0.55
Interface	-	1.00×10^{-4}	0.31

Equivalent circuits consist of a combination of resistive elements (R), inductors (L), and reactive elements such as capacitors (C) or constant phase elements (CPE) connected in series or parallel [10, 11]. Each component in the circuit is representative of a different physical

process inside the sample. CPEs are regarded as leaky capacitors or capacitors with a resistive component and represent deviations from an ideal capacitive behavior [12-15]. The impedance of the constant phase element is given by

$$Z^*_{CPE} = \frac{1}{A(j\omega)^n} \quad (3.1)$$

Where *A* and *n* are constants and $j = \sqrt{-1}$. '*n*' in formula 3.1 varies between 0 and 1 with 0 representing a pure resistor and 1 an ideal capacitor.

The equivalent circuit shown as the inset of Fig. 3.6(c) was employed to analyze the impedance data for NNCM. The fitted values of circuit elements R1, R2, CPE1, CPE2, and CPE3 (Table 3.3) confirmed that the large semi-circle seen in the Nyquist plots with large capacitive and resistance values corresponds to grain boundaries. The poorly resolved arc in higher frequency regions arises from grains. Therefore, the parallel combination of R1 and CPE1 in the model represents the grains, R2 & CPE2 (Table 3.2) represent the highly resistive grain boundaries, and the element CPE3 represents the highly capacitive sample-electrode interface region. Further, the values of *n* associated with the element CPE1 was ~ 0.97, and that for the element CPE2 was ~ 0.5 at all temperatures. This indicate that the conductivity relaxation in the grains has a comparatively much lesser deviation from the ideal Debye behaviour than that in grain boundary regions [15].

The values of room temperature DC conductivity of the grains and grain boundaries were calculated using the fitted values of R1, R2 and sample dimensions ($\sigma = t/(R \times A)$; *t* is the thickness of pellet and *A* is the area of cross-section of the pellet) and were found to be about $(5.25 \pm 0.05) \times 10^{-5}$ Scm^{-1} and $(4.70 \pm 0.03) \times 10^{-6}$ Scm^{-1}, respectively.The total conductivity of the sample was calculated to be about $(4.28 \pm 0.08) \times 10^{-6}$ Scm^{-1}.

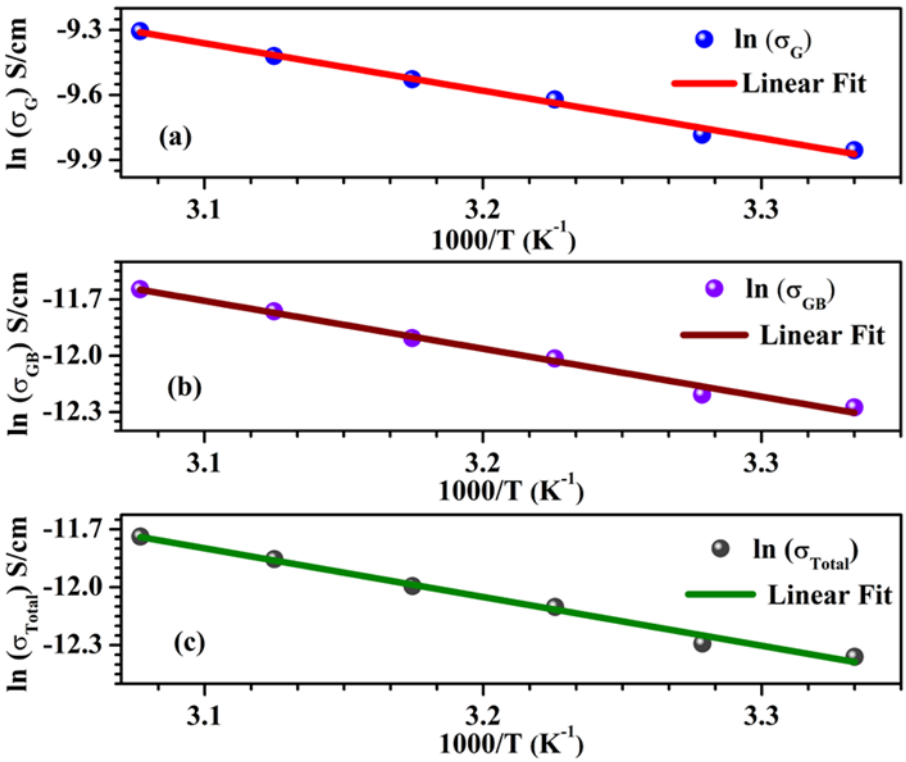

Figure 3.7. Arrhenius plots showing temperature dependence of (a) grain conductivity σ_G, (b) grain boundary conductivity σ_{GB}, and (c) total conductivity σ_{total}.

The DC conductivities of both grains and grain boundaries are temperature-dependent and show an increasing trend with the increase in temperature. Activation energies (E_A) for grain and grain boundary regions, temperature-dependent conductivity values were fitted using the Arrhenius equation.

$$\sigma(T) = \sigma_o \, e^{-(\frac{E_A}{kT})} \qquad (3.2)$$

where σ_0 is the pre-exponential factor, k is Boltzmann's constant, and T is the absolute temperature (Fig. 3.7).

Table 3.3. DC conductivities, activation energies, and diffusion coefficients of grain, grain boundary, and overall sample (total) at room temperature.

Component	DC Conductivity (Scm^{-1})	Activation Energy (eV)	Diffusion Coefficient (m^2s^{-1})
Grain	$(5.25 \pm 0.05) \times 10^{-5}$	0.189 ±0 .008	4.91×10^{-14}
Grain Boundary	$(4.70 \pm 0.03) \times 10^{-6}$	0.22 ± 0.01	4.39×10^{-15}
Total	$(4.28 \pm 0.08) \times 10^{-6}$	0.21 ± 0.01	4.00×10^{-15}

All three DC conductivities (grain conductivity σ_G, grain boundary σ_{GB} and total conductivity σ_{total}) show an almost linear trend in the Arrhenius plot confirming that the conduction process in NNCM is thermally activated. The RT values of activation energies along with the diffusion coefficients (D) estimated using the Nernst Einstein relation (eq. 3.3) are provided in Table 3.3.

$$D = \frac{kT}{Nq^2}\ \sigma_{DC} \tag{3.3}$$

Where N is the number density of charge carriers per unit volume of the unit cell and q is the elementary charge. The diffusion coefficients calculated through the galvanostatic intermittent titration technique (GITT) for different P2 type cathodes reported in the literature are shown in Table 3.4.

Table 3.4. Na^+ diffusion coefficients in various P2 type layered oxides.

Compound	Diffusion Coefficient (m^2s^{-1})	Ref.
$\mathbf{Na_{0.67}Mn_{0.65}Ni_{0.2}Co_{0.15}O_2}$	1.0×10^{-18}	[16]

$Na_{0.6}Co_{0.1}Mn_{0.9}O_2$	1×10^{-17}	[17]
$Na_{0.67}Mn_{0.55}Ni_{0.25}Li_{0.2}O_2$	9.81×10^{-18}	[18]
$Na_{2/3}Ni_{1/3}Mn_{5/9}Al_{1/9}O_2$	2.5×10^{-16}	[6]
$Na_{0.5}Mg_{0.02}Ni_{0.15}Mn_{0.83}O_2$	5.4×10^{-14}	[19]
$Na_{2/3}Fe_{2/3}Mn_{1/3}O_2$	1.3×10^{-16}	[20]
$Na_{2/3}Cu_{1/12}Ni_{1/4}Mn_{2/3}O_2$	1.0×10^{-16}	[21]
$Na_{0.70}Ni_{0.20}Cu_{0.15}Mn_{0.65}O_2$	4.9×10^{-14}	This work

To confirm the ion conduction indicated by the tail component in the Nyquist plots, chronoamperometry was performed on the sample at room temperature under an applied DC voltage of 1 V. As displayed in Fig. 3.8, the initial value of the current (I_0) is around 126.6 μA and a steady current close to 16.6 μA is recorded after the exponential decay.

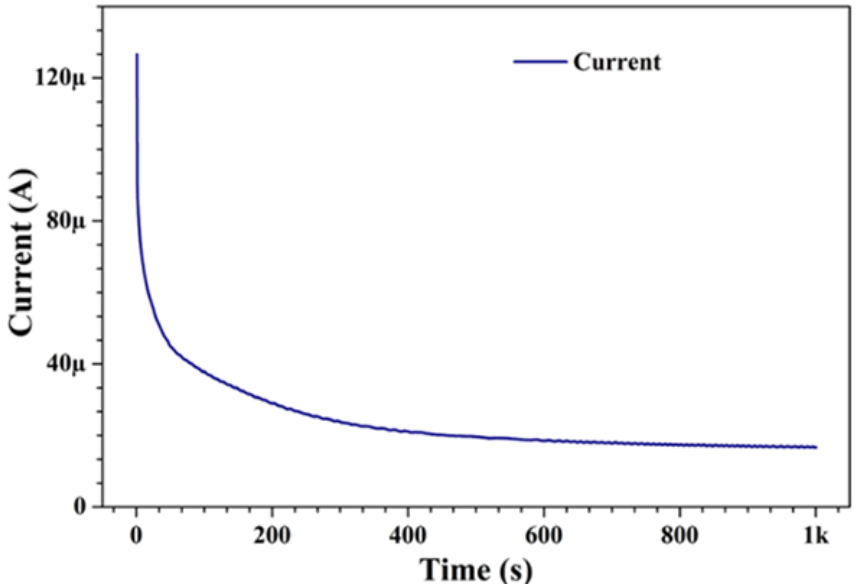

Figure 3.8. Variation of current with time under an applied potential of 1 V.

transference number coupled with the high value of room temperature conductivity (of order 10^{-4} S/cm) in grain region indicates facile

sodium ion conduction in NNCM crystal structure. The room temperature grain electronic conductivity of NNCM is estimated to be about 7.35×10^{-6} S/cm.

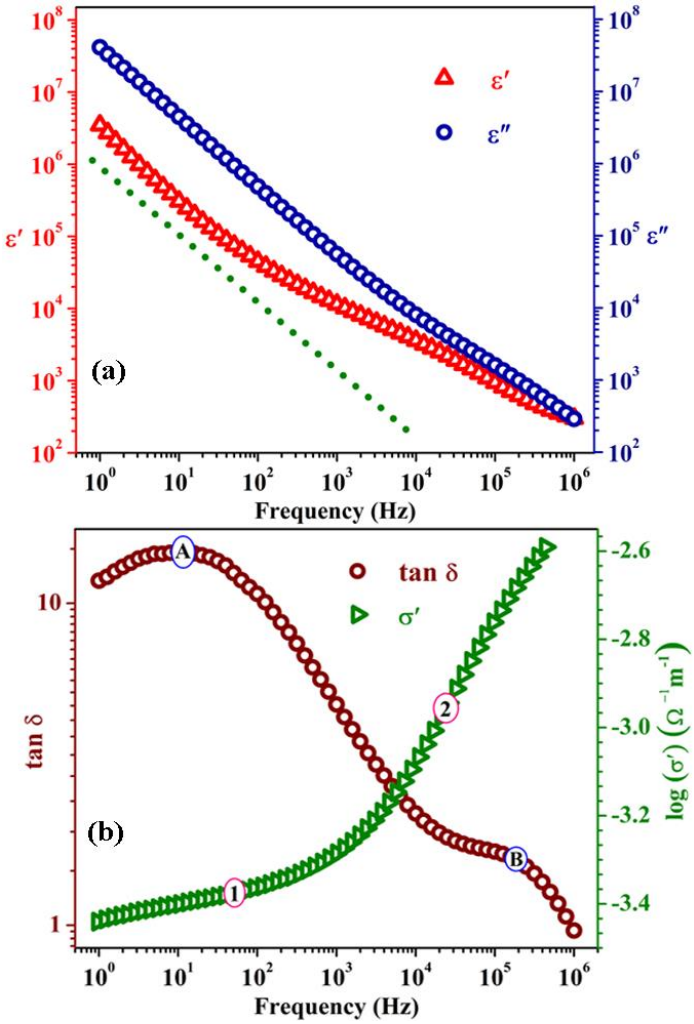

Figure 3.9. (a) ε′ and ε″ versus frequency plot at 300 K. The dotted line represents a slope of -1 (b) Conductivity (σ′) and tan δ versus frequency plots at 300 K.

To further elucidate the relaxations associated with the Na-ions in NNCM, frequency variation of real and imaginary parts of dielectric permittivity (calculated using equations (3.5) and (3.6) was studied.

$$\varepsilon^* = \varepsilon' - j\varepsilon'' \tag{3.4}$$

$$\varepsilon' = \frac{Z''}{\omega C_0 (Z'^2 + Z''^2)} \tag{3.5}$$

$$\varepsilon'' = \frac{Z'}{\omega C_0 (Z'^2 + Z''^2)} \tag{3.6}$$

Where ε′ and ε″ are the real and imaginary parts of the dielectric permittivity, $j = \sqrt{-1}$, ω ($2\pi f$) is the angular frequency and C_0 is the capacitance of the sample. ε′ is representative of the capacitance and polarization in the sample, while ε″ indicates dielectric loss and conductance within the sample [22]. The loss tangent (tan δ), given by ε″/ ε′ and the real part σ′ (= $\omega\varepsilon_0\varepsilon''$) of the complex ionic conductivity have also been calculated and plotted against frequency (*f*) as shown in Fig. 3.9 (b). At 1 Hz, both ε′ and ε″ (Fig. 3.9 (a), at 300 K) show a value close to 10^8, which decreases exponentially with the increase in frequency. The high dielectric constant values at low frequencies indicate high space-charge polarization caused by the blocking of Na-ions at the sample-electrode interface [22]. The slope of ε″ versus *f* curve is almost equal to -1 at low and intermediate frequencies, which suggests a high dc conduction through the sample [15, 22]. Further evidence for both the electrode polarization and dc conduction can be seen in the σ′ versus *f* plot (Fig. 3.9(b)). The decrease in ac conductivity values in the low-frequency regime (shown as 1) is attributed to the electrode polarization [23]. The deviation observed from the above-discussed trend in both the ε′ versus *f and* ε″ versus *f* curves at frequencies above 10^4 Hz is due to the relaxation of Na^+ ions in the grains, which normally occurs at high frequencies due to their low resistance towards electrical conduction. Typically, such relaxation causes a step-like drop in the ε′ versus frequency plot centered around a characteristic relaxation frequency which is accompanied by a peak in ε″ versus frequency plot at the same relaxation frequency. In NNCM, dominating effects of high values of dc conductivity and a strong electrode polarisation, especially at lower frequencies, suppress the grain boundaries relaxation related features in frequency variation of the dielectric permittivity. Accordingly, no peaks in the ε″ versus frequency plot are apparent in Fig. 3.9. However, the peaks relating to grain (depicted as B in Fig. 3.9 (b)) and grain boundary (depicted as A) relaxations are clearly observed in the

tan δ versus *f* curve in high and low frequencies regions, respectively [24].

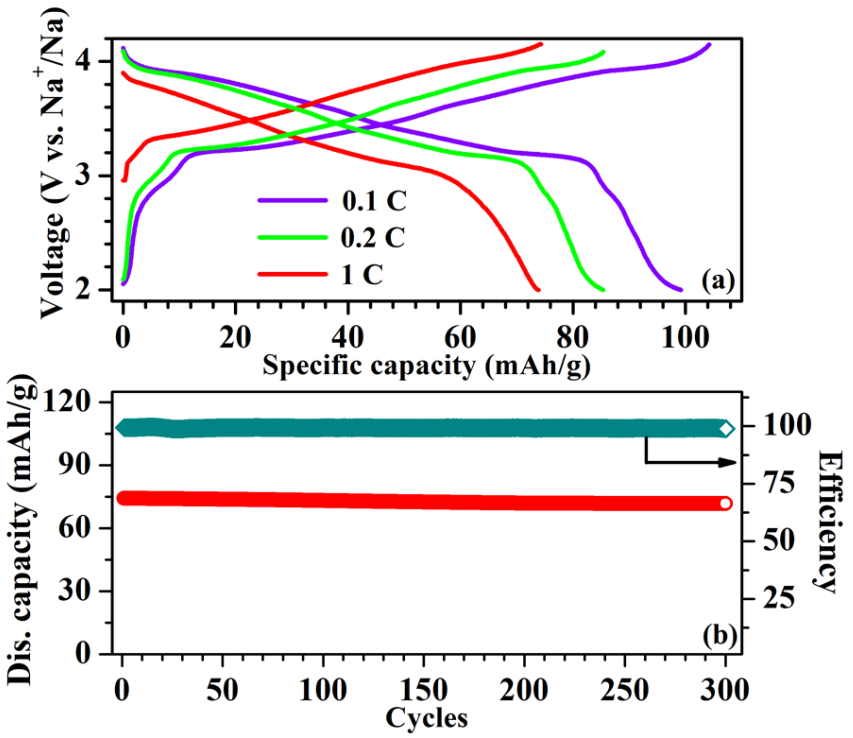

Figure 3.10. (a) Galvanostatic charge-discharge curves of NNCM samples at discharge rates of 0.1C, 0.2C and 1C. (b) Cyclic performance of the NNCM samples at 1C for 300 cycles.

3.4. Electrochemical properties

The galvanostatic charge/discharge (GCD) profiles of the NNCM cathode cycled between 2.00 – 4.25 V (vs. Na/Na^+) at discharge rates of 0.1C, 0.2C, and 1C are displayed in Fig. 3.10 (a). At a discharge rate of 0.1C, the sample showed a specific capacity of 99 mAh/g, which decreased to 74 mAh/g at 1C. All the profiles show a decreased slope between 3 – 4 V, while a higher slope is observed between 2 – 3 V. This is because the $Ni^{2+/4+}$ and $Cu^{2+/3+}$ redox couples are active between 3 – 4 V; hence the cell shows most of its capacity in this voltage range [25, 26]. In terms of cyclic performance, the cell retained 95% of its initial capacity after 300 cycles when cycled at 1C (Fig. 3.10(b)),

making it an attractive material as a cathode for Na-ion batteries for long-term stationary storage applications.

3.5. References

[1] P.-F. Wang, H.-R. Yao, X.-Y. Liu, Y.-X. Yin, J.-N. Zhang, Y. Wen, X. Yu, L. Gu, Y.-G. Guo, Science Advances, 4 (2018) eaar6018.

[2] D.H. Lee, J. Xu, Y.S. Meng, Physical Chemistry Chemical Physics, 15 (2013) 3304-3312.

[3] R. Berthelot, D. Carlier, C. Delmas, Nature Materials, 10 (2011) 74-80.

[4] A. Coelho, Journal of Applied Crystallography, 51 (2018) 210-218.

[5] X.-H. Zhang, W.-L. Pang, F. Wan, J.-Z. Guo, H.-Y. Lü, J.-Y. Li, Y.-M. Xing, J.-P. Zhang, X.-L. Wu, ACS applied materials & interfaces, 8 (2016) 20650-20659.

[6] K. Momma, F. Izumi, Journal of Applied Crystallography, 44 (2011) 1272-1276.

[7] J.F. Moulder, J. Chastain, Handbook of X-ray Photoelectron Spectroscopy: A Reference Book of Standard Spectra for Identification and Interpretation of XPS Data, Physical Electronics Division, Perkin-Elmer Corporation, 1992.

[8] S. Hüfner, Photoelectron spectroscopy: principles and applications, Springer Science & Business Media, 2013.

[9] A.R.C. Bredar, A.L. Chown, A.R. Burton, B.H. Farnum, ACS Applied Energy Materials, 3 (2020) 66-98.

[10] W. Woodward, Broadband Dielectric Spectroscopy—A Practical Guide, in, 2021, pp. 3-59.

[11] L.A. Middlemiss, A.J.R. Rennie, R. Sayers, A.R. West, Energy Reports, 6 (2020) 232-241.

[12] S. Kumar, K.B.R. Varma, Journal of Physics D: Applied Physics, 42 (2009) 075405.

[13] M.A. Hernández, N. Masó, A.R. West, Applied Physics Letters, 108 (2016) 152901.

[14] E. von Hauff, Journal of Physical Chemistry C, 123 (2019) 11329-11346.

[15] Z.-Y. Li, R. Gao, L. Sun, Z. Hu, X. Liu, Journal of Materials Chemistry A, 3 (2015) 16272-16278.

[16] Z.-Y. Li, R. Gao, L. Sun, Z. Hu, X. Liu, Journal of Materials Chemistry A, 3 (2015) 16272-16278.

[17] N. Bucher, S. Hartung, J.B. Franklin, A.M. Wise, L.Y. Lim, H.-Y. Chen, J.N. Weker, M.F. Toney, M. Srinivasan, Chemistry of Materials, 28 (2016) 2041-2051.

[18] Z.-Y. Li, J. Zhang, R. Gao, H. Zhang, L. Zheng, Z. Hu, X. Liu, The Journal of Physical Chemistry C, 120 (2016) 9007-9016.

[19] L.A. Ma, R. Palm, E. Nocerino, O.K. Forslund, N. Matsubara, S. Cottrell, K. Yokoyama, A. Koda, J. Sugiyama, Y. Sassa, M. Månsson, R. Younesi, Physical Chemistry Chemical Physics, 23 (2021) 24478-24486.

[20] N.A. Katcho, J. Carrasco, D. Saurel, E. Gonzalo, M. Han, F. Aguesse, T. Rojo, Advanced Energy Materials, 7 (2017) 1601477.

[21] L. Zheng, J. Li, M. Obrovac, Chemistry of Materials, 29 (2017) 1623-1631.

[22] S. Kumar, K.B.R. Varma, Current Applied Physics, 11 (2011) 203-210.

[23] S. Corezzi, S. Capaccioli, G. Gallone, M. Lucchesi, P.A. Rolla, Journal of Physics: Condensed Matter, 11 (1999) 10297-10314.

[24] D.M. Abdel-Basset, S. Mulmi, M.S. El-Bana, S.S. Fouad, V. Thangadurai, Inorganic Chemistry, 56 (2017) 8865-8877.

[25] K. Tang, Y. Huang, X. Xie, S. Cao, L. Liu, H. Liu, Z. Luo, Y. Wang, B. Chang, H. Shu, X. Wang, Chemical Engineering Journal, 399 (2020) 125725.

[26] Q. Pei, M. Lu, Z. Liu, D. Li, X. Rao, X. Liu, S. Zhong, ACS Applied Energy Materials, 5 (2022) 1953-1962.

Enhanced Rate Performance and Specific Capacity in Ti-Substituted P2-Type Layered Oxide Through Structural Modifications

This chapter reports on the effects of structural changes in $Na_{0.70}Ni_{0.20}Cu_{0.15}Mn_{(0.65-x)}Ti_xO_2$ (hereinafter, NNCMT-*x*, *x* = 0, 0.025, 0.050, 0.075, and 0.100) on the electrochemical behaviour of these samples. To rationalize the improvement in electrochemical performance, the electrical properties have also been investigated by performing complex impedance spectroscopy and chronoamperometry on each of the samples. In addition, ex-situ XRD analysis was also conducted on the samples at different stages of the charge/discharge cycle to identify the structural changes in the cathodes during cycling.

4.1. XRD

Figure 4.1 shows the phase evolution of NNCMT-*x (x* = 0, 0.050, and 0.100*)* with the increase in calcination temperature. The XRD patterns show a rise in the intensity of peaks relating to the P2-type phase with the increase in calcination temperatures. Sample with the composition corresponding to *x* = 0.100 shows a minor O3 phase which is estimated to be about 3 wt. % of the sample. At calcination temperatures above 900 °C, a small CuO impurity phase was found in the Ti substituted samples. Initial analysis of the XRD patterns showed that Ti substitution was effective in decreasing the calcination temperatures of the parent material. The optimal calcination temperature decreases from 850 °C for *x* = 0 & 0.025 samples to 800 °C for samples with *x* = 0.05, 0.075, and 0.100.

The Rietveld refinement of the XRD data was utilized to determine the crystal structure of as-prepared NNCMT samples. The experimental data along with the refinement profiles for two representative samples (x = 0 and x = 0.075) are shown in Fig. 4.2 and for x = 0.025, 0.050, and 0.100 samples are provided in the Supplementary Information (Fig. 4.3). The refinement of the XRD data confirms that all samples crystallize in the P2-type phase with hexagonal symmetry ($P6_3/mmc$ space group).

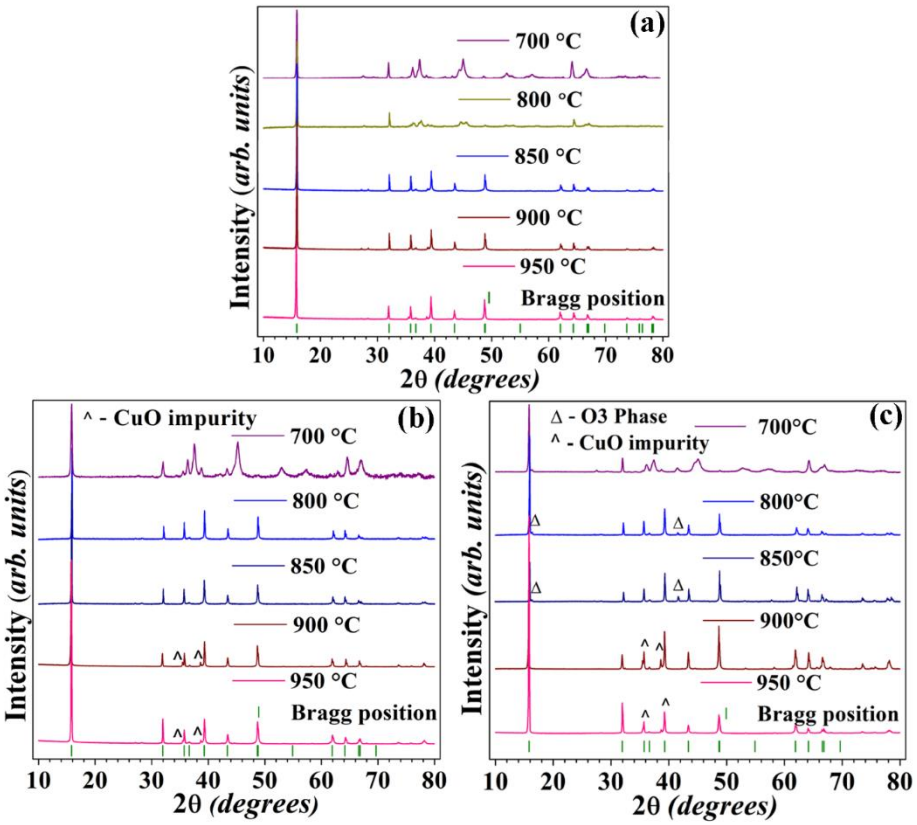

Figure. 4.1. XRD patterns showing the phase evolution of (a) x = 0, (b) x = 0.050, and (c) x = 0.100 samples with calcination temperature

A few minor peaks associated with the O3-type phase are also observed in the XRD pattern of the x = 0.100 sample. The weight fraction of the O3 phase in this sample was estimated to be ~ 5 % of the sample. The two minor peaks at ~ 27.2° and 28.3° in the XRD pattern of the x = 0 sample (marked by the * symbol in Fig. 4.2) correspond to superlattice reflections caused by the in-place Na-ion vacancy ordering [1-3]. Vacancy ordering of Na-ions in layered oxides is known to hider Na-ion diffusion and induce phase transformations

during the cycling [4, 5]. The intensities of these peaks decreased gradually with the increase in Ti concentration suggesting the successful suppression of Na-ion vacancy ordering by Ti-ions in the material which concurs with the findings reported in the literature [6, 7].

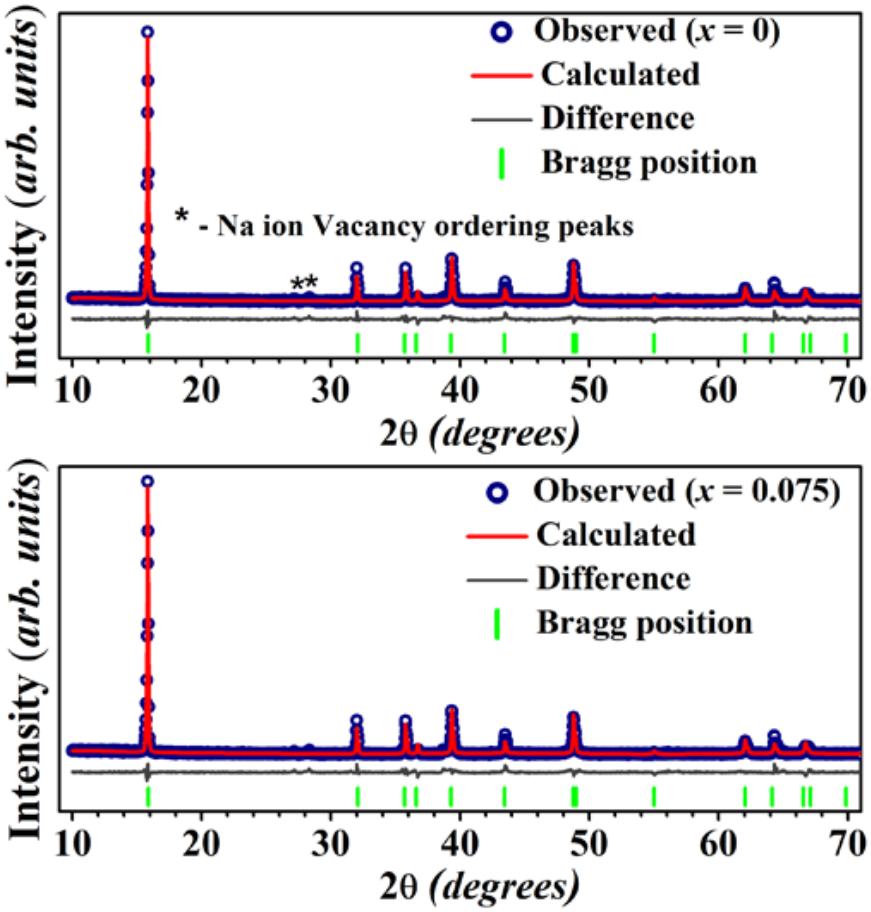

Figure. 4.2. Rietveld refinement profiles of room temperature XRD data for x = 0 and 0.075 samples calcined at 850 °C and 800 °C, respectively.

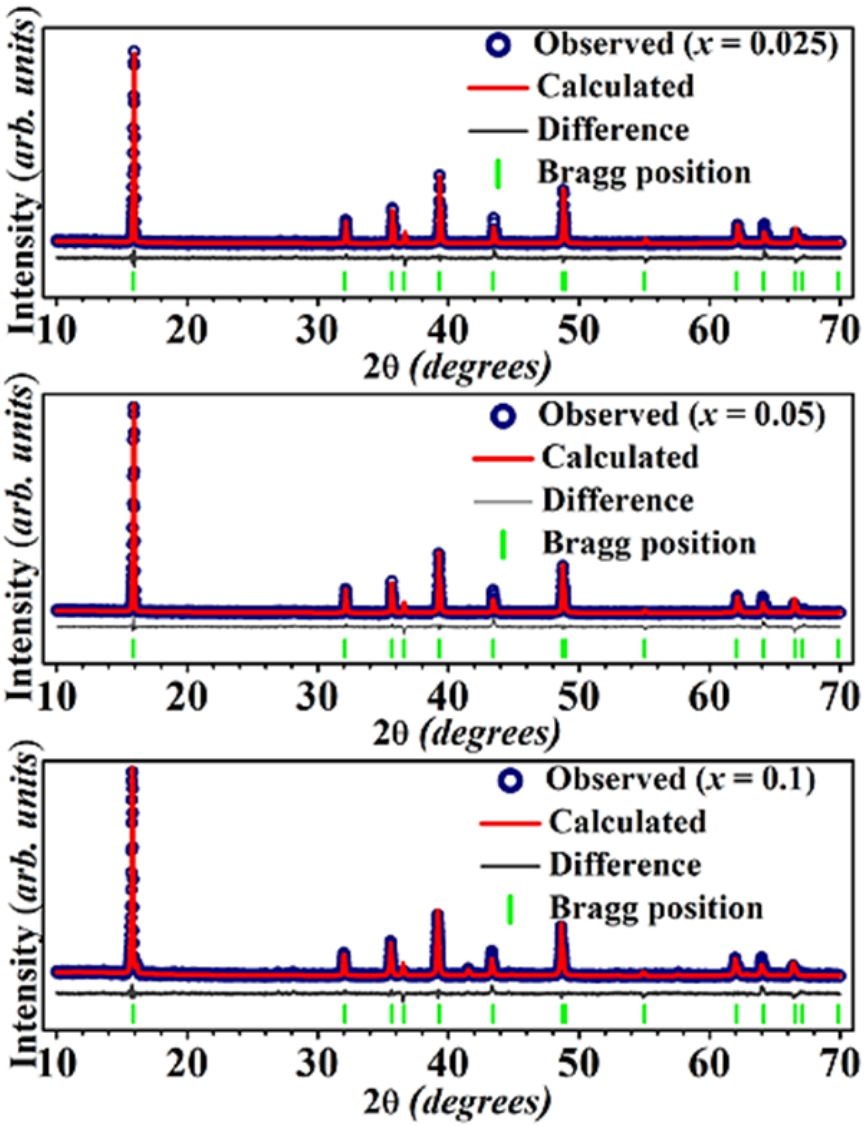

Figure. 4.3. Rietveld refinement profiles of room temperature XRD data of *x* = 0.025 calcined at 850 °C , *x* = 0.050 calcined at 800 °C and *x* = 0.100 calcined at 800 °C.

Various crystallographic parameters obtained from the Rietveld refinement of the XRD data for all samples are provided in Tables 4.1 and Tables 4.2 - 4.7. An increase in the lattice parameter *a*, a decrease in the lattice parameter *c*, and an overall increase in volume *V* of the hexagonal unit cell are seen with the increase in the concentration of Ti in NNCMT-*x*. This is due to the smaller size of Ti^{4+} (0.605 Å in 6 coordination) compared to the Mn^{4+} (0.656 Å in 6 coordination) [6, 8, 9]. Further analysis of the XRD data revealed an increase in the area of the lateral faces of Na-O_6 prisms (Fig. 4.4) with the increase in Ti

concentration. Accordingly, the rectangular bottleneck for the sodium intercalation at the Na1 site increased from 11.03 $Å^2$ for NNCMT-0 to 11.47 $Å^2$ for the NNCMT-0.100 sample. In addition, the volume of TM-O_6 octahedron for NNCMT-0 is calculated to be ~ 8.53 $Å^3$ which decreases to ~ 8.36 $Å^3$ for the 10% Ti-doped sample, whereas, the volume of the Na-O_6 prisms increased from 13.83 $Å^3$ to 14.09 $Å^3$. Similar expansions of Na-O_2 layers accompanied by contractions of TM-O_2 layers upon Ti-substitution for Mn in layered oxides has been observed in earlier work [1]. The increase in the area of the lateral faces of Na-O_6 prisms is significant as it is expected to facilitate the conduction of Na-ions through the material by increasing the size of the rectangular bottleneck formed by the oxygen ions. This is substantiated by the improvement in electrical properties of the Ti-doped samples (discussed later in the text).

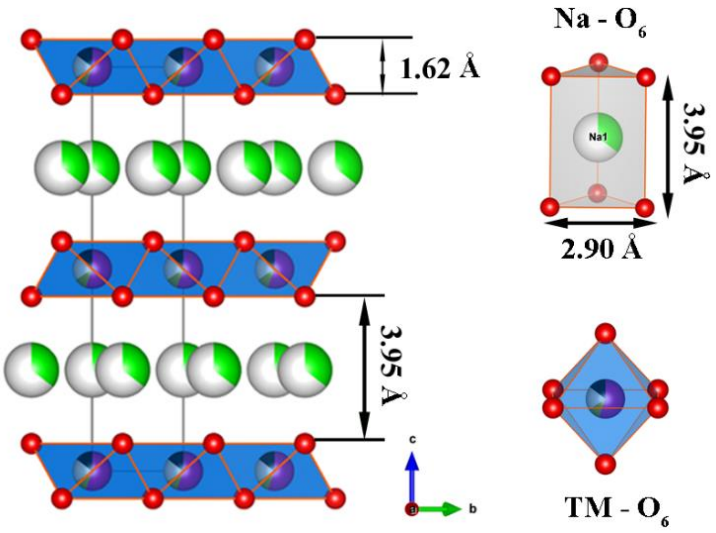

Figure. 4.4. Crystal structure of P2-type NNCMT-0.1 visualized using VESTA software package [10].

Table 4.1. Lattice parameters of NNCMT-x samples obtained from Rietveld refinement of room temperature XRD data.

Sample		***a* (Å)**	***c* (Å)**	***V* (Å^3)**	**Reliability Factors**
***x* = 0**		2.8934 ± 0.0001	11.1660 ± 0.0004	80.9559 ± 0.0007	Rexp : 2.02 Rwp : 3.82 Rp : 2.65 GOF : 1.89
***x* = 0.025**		2.9006 ± 0.0004	11.1357 ± 0.0002	81.1400 ± 0.0003	Rexp : 2.49 Rwp : 4.27 Rp : 2.86 GOF : 1.72
***x* = 0.050**		2.9044 ± 0.0006	11.1318 ± 0.0003	81.3260 ± 0.0004	Rexp : 2.47 Rwp : 4.50 Rp : 2.88 GOF : 1.82
***x* = 0.075**		2.9063 ± 0.0004	11.1276 ± 0.0002	81.4002 ± 0.0003	Rexp : 2.57 Rwp : 4.69 Rp : 2.99 GOF : 1.82
***x* = 0.100**	P2(96.4 %)	2.9041 ± 0.0007	11.1485 ± 0.0004	81.4290 ± 0.0005	Rexp : 2.60 Rwp : 4.19 Rp : 2.90 GOF : 1.62
	O3 (3.6%)	2.9525 ± 0.0006	16.3764 ± 0.0004	123.6342 ± 0.0006	

Tables S1-S6. Crystallographic parameters of P2-type NNCMT-*x* obtained from Rietveld refinement of room temperature XRD data.

4.2: *x* = 0 (space group: *P*6$_3$/*mmc*)						
	x	**y**	**z**	**Occupancy**	**Site**	**B**
Na1	2/3 **Atom**	1/3	¼	0.45	2d	1
Na2	0	0	¼	0.25	2b	1
Mn/ Ti/ Ni/ Cu	0	0	0	0.65/0 /0.20/0.15	2a	1
O	2/3	1/3	0.079	1	4f	1
4.3: *x* = 0.025 (space group: *P*6$_3$/*mmc*)						
Atom	**x**	**y**	**z**	**Occupancy**	**Site**	**B**
Na1	2/3	1/3	¼	0.45	2d	1
Na2	0	0	¼	0.25	2b	1
Mn/ Ti/ Ni/ Cu	0	0	0	0.625/0.025/0. 20/0.15	2a	1
O	2/3	1/3	0.078	1	4f	1
4.4: *x* = 0.050 (space group: *P*6$_3$/*mmc*)						
Atom	**x**	**y**	**z**	**Occupancy**	**Site**	**B**
Na1	2/3	1/3	¼	0.45	2d	1
Na2	0	0	¼	0.25	2b	1
Mn/ Ti/ Ni/ Cu	0	0	0	0.60/0.05/0.20/ 0.15	2a	1
O	2/3	1/3	0.078	1	4f	1

4.5: x = 0.075 (space group: $P6_3/mmc$)

Atom	x	y	z	Occupancy	Site	B
Na1	2/3	1/3	¼	0.45	2d	1
Na2	0	0	¼	0.25	2b	1
Mn/ Ti/ Ni/ Cu	0	0	0	0.575/0.075/0.20/0.15	2a	1
O	2/3	1/3	0.077	1	4f	1

4.6: x = 0.100 (space group: $P6_3/mmc$), phase fraction = 96.4%

Atom	x	y	z	Occupancy	Site	B
Na1	2/3	1/3	¼	0.45	2d	1
Na2	0	0	¼	0.25	2b	1
Mn/ Ti/ Ni/ Cu	0	0	0	0.55/0.1/0.20/0.15	2a	1
O	2/3	1/3	0.077	1	4f	1

4.7: x = 0.100 (space group: R-3m) phase fraction = 3.6%

Atom	x	y	z	Occupancy	Site	B
Na1	0	0	½	0.70	3b	1
Mn/ Ti/ Ni/ Cu	0	0	0	0.55/0.1/0.20/0.15	3a	1
O	0	0	0.258	1	6c	1

4.2. Microstructure

The SEM micrographs of x = 0, 0.050, and 0.075 samples along with the representative elemental maps for the x = 0.075 sample are shown in Fig. 4.5 The SEM images for the x = 0.025 and 0.100 are given in Fig. 4.6. The elemental mapping indicates a uniform distribution of all

the elements throughout the sample without any noticeable segregation. The SEM micrographs show a distinct change in morphology of powder particles with the increase in Ti substitution. The parent material was observed to have thinner hexagonal plates with sharper facets and large aspect ratios (close to 8) while the Ti substituted samples show thicker particles with rounded edges and lower aspect ratios (close to 1). The average particle size (in the bigger (001) surface) was estimated to decrease from ~ 1.9 μm for the undoped (x = 0) sample to ~ 0.9 μm for the x = 0.075 sample, while the average thickness increased from ~ 0.25 μm in the former to ~ 0.85 μm in the latter.

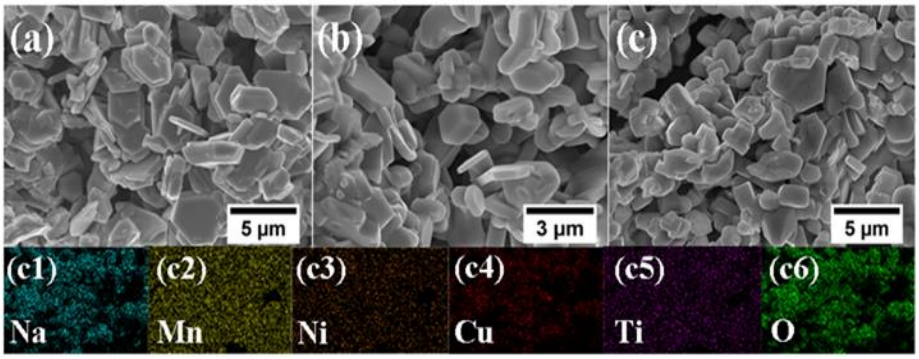

Figure. 4.5. SEM micrographs of (a) x = 0, (b) x = 0.05, and (c) x = 0.075 samples. (c1)-c(6) EDS maps of x = 0.075 showing the distribution of its constituent elements.

The hexagonal plate-type morphology of the NNCMT sample can be explained by the relatively lower surface energy of (001) and $(00\bar{1})$ surfaces as compared to (100), (010), (110), $(\bar{1}00)$, $(0\bar{1}0)$, and $(\bar{1}\bar{1}0)$ surfaces. Accordingly, the equilibrium shape of NNCMT crystals will be dominated by (001) and $(00\bar{1})$ surfaces resulting in a hexagonal plate-like morphology with a large aspect ratio (Fig. 4.5(a)). The change in the morphology of the Ti substituted samples suggests that the61ntroducetion of Ti^{4+} ions could increase the relative surface energies of (001) and $(00\bar{1})$ surfaces, and consequently, a decrease in the aspect ratios. It should be noted that in P2-type material, the diffusion of Na-ion is predominantly in the basal planes. The increase in relative area of (100), (010), (110), $(\bar{1}00)$, $(0\bar{1}0)$, and $(\bar{1}\bar{1}0)$ surfaces

is expected to facilitate faster Na-ion intercalation which should result in better rate performances of the cathode material.

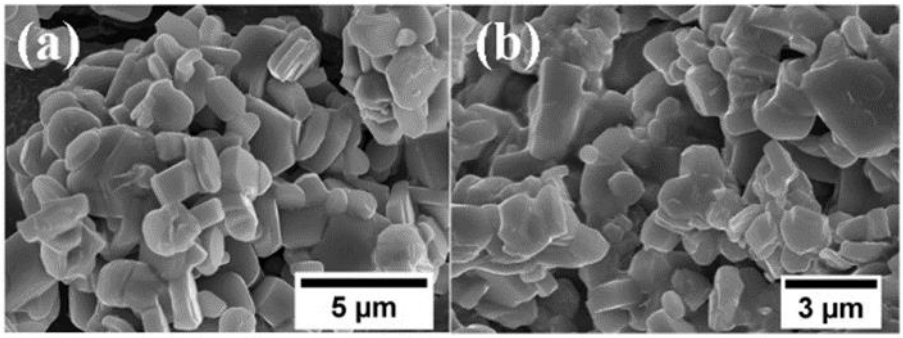

Figure. 4.6. SEM micrographs of (a) *x* = 0.025 and (b) x = 0.100 samples

4.3. XPS

X-ray photoelectron spectroscopy (XPS) was performed to verify the oxidation states of constituent transition metals in NNCMT samples. Figure 4.7 compares the XPS spectra of Ni 2p, Mn 2p, Cu 2p, and Ti 2p in different samples. The four characteristic peaks in the Ni2p spectra are attributed to Ni $2p_{3/2}$ (~ 855 eV) and Ni $2p_{1/2}$(~ 872 eV) and their shake-up satellite peaks indicate that Ni maintained a +2 oxidation state in all samples [11-13]. The two peaks in the Cu 2p spectra centered at ~ 933 and ~ 953 eV correspond to Cu $2p_{3/2}$ and $Cu2p_{1/2}$, respectively, suggesting that Cu also has a +2 oxidation in all the materials [11-13]. The Mn 2p spectra can be deconvoluted into 2 peaks at ~ 643 eV (Mn $2p_{3/2}$) and ~ 654 eV (Mn $2p_{1/2}$) confirming the existence Mn^{4+} ions in the samples [11-13]. The Ti $2p_{3/2}$ and Ti $2p_{1/2}$ peaks located at 458 and 464 eV in the Ti 2p spectra indicate the presence of Ti^{4+} ions in the Ti-doped samples [12, 13]. The XPS spectra of all other elements in the Ti-doped samples were found to be identical to that of the parent composition indicating that Ti doping did not affect the oxidation states of any of the elements present in these samples.

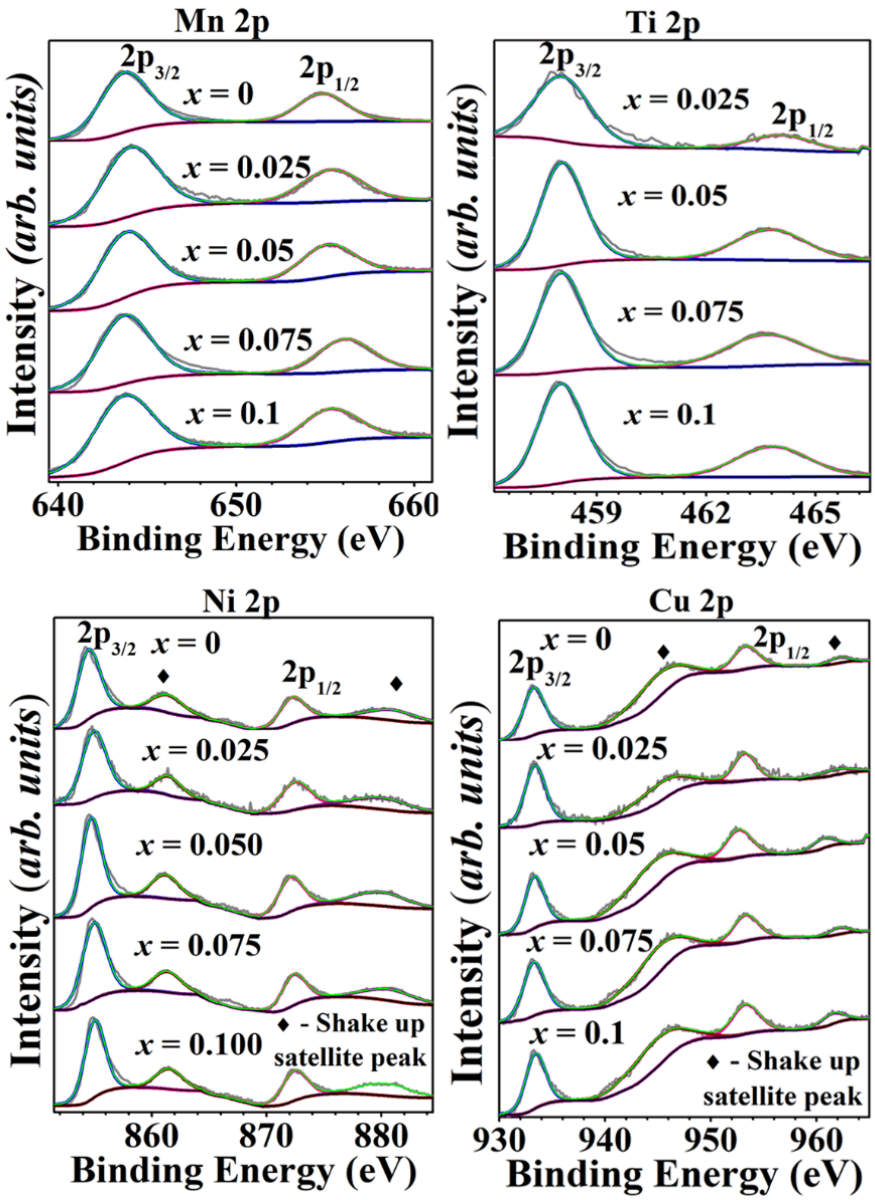

Figure. 4.7. XPS spectra of as-prepared $Na_{0.67}Ni_{0.20}Cu_{0.15}Mn_{(0.65-x)}Ti_xO_2$ samples (x = 0, 0.025, 0.050, 0.075, 0.100).

4.4. Cyclic Voltammetry

To investigate the redox process in the prepared cathode materials, cyclic voltammetry (CV) was performed on the half-cells between a potential window of 2.00 - 4.25 V with a scan rate of 0.1 mV/s.

The CV profiles of the first 3 cycles for the x = 0 and 0.075 samples are shown in Fig. 4.8 and that of x = 0.025, 0.050, and 0.100 are given in Fig. 4.9. The minor peaks observed below 3 V for all cathodes can be related Mn^{3+}/Mn^{4+} redox processes [14, 15].

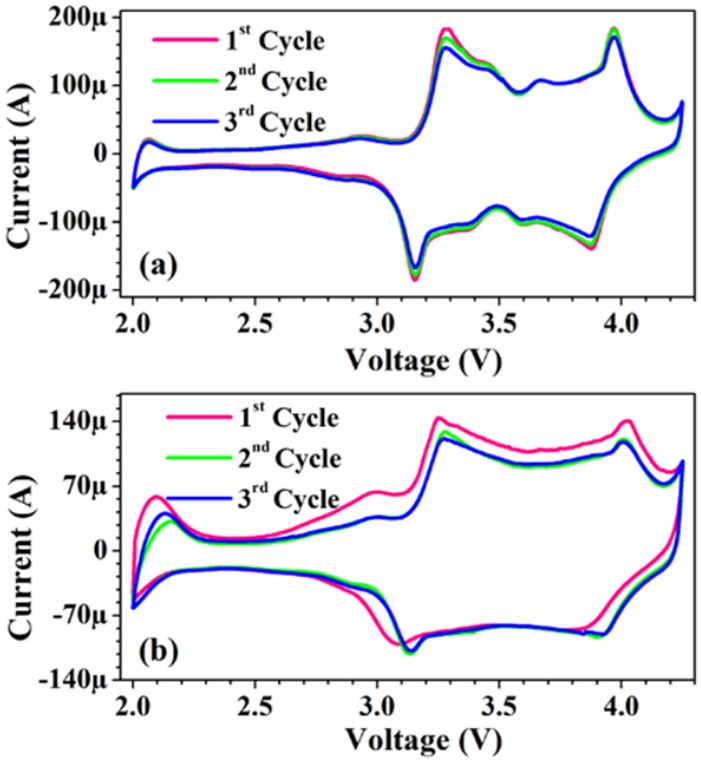

Figure. 4.8. Cyclic voltammogram of (a) x = 0 and (b) x = 0.075 samples at scan rate of 0.1 mv/s.

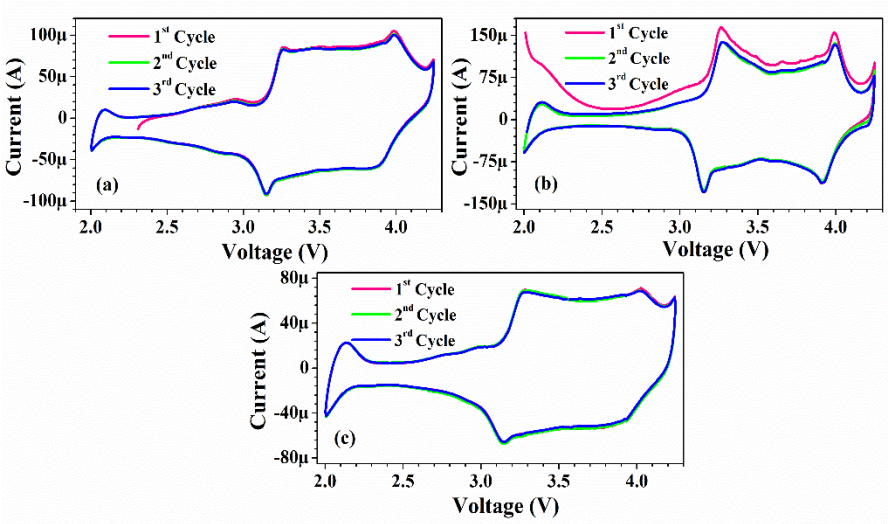

Figure. 4.9. Cyclic voltammogram of (a) x = 0.025, (b) x = 0.050, and (c) x = 0.100 sample at scan rate of 0.1 mV/s.

As mentioned before, Ti^{4+} ions do not show any redox activity in the 2.00 - 4.25 V potential range and, hence, remain largely electrochemically inactive [7, 16]. For x = 0 sample, two peaks centred at ~ 3.45 V and ~ 3.68 V are attributed to Ni^{2+}/Ni^{4+} redox reaction and

Na-ion vacancy ordering [6, 7]. In contrast, Ni^{2+}/Ni^{4+} redox peaks in the Ti substituted samples are located at ~ 3.2 V, and the peaks related to Na-ion vacancy ordering almost vanish which concurs with the observed decrease in the intensity of the vacancy ordering related superlattice reflections in the XRD patterns. The peak observed at ~ 3.95 V is related to the oxidation of Cu ions from 2+ to 3+. The CV profiles for the second and third cycles of all the cathodes almost coincided with each other indicating excellent reversibility of all the redox processes.

4.5. Galvanostatic Charge/Discharge

The galvanostatic charge/discharge (GCD) profiles of all samples between 2.00 – 4.25 V at discharge rates of 0.1C and 1C are displayed in Fig. 4.10 (a) & (b). The discharge profiles show a slow voltage drop with an increase in capacity between 4 V to 3 V where $Ni^{4+/2+}$ and $Cu^{3+/2+}$ redox activity was observed in the CV profiles. The voltage drop becomes more drastic between 3 V to 2 V due to the smaller number of $Mn^{4+/3+}$ redox couples. It is interesting to note that all the Ti substituted samples exhibited higher specific capacities compared to the unsubstituted sample at different discharge rates. At 0.1C rate, x = 0.1 and 0.075 samples showed a specific capacity of ~ 127 mAh/g which is about 28% more than the unsubstituted sample (i.e., composition with x = 0). As the discharge rate was increased from 0.1C to 1C, the x = 0.075 sample showed the lowest drop in specific capacity among all samples. The specific capacity is close to 97 mAh/g which is about 31% more than that of the unsubstituted sample at the same discharge rate of 1C. These results are significant as Ti ions being lighter than their Mn counterparts were estimated to increase the specific capacity by a margin of only 2-3 % but an increase in 27% of specific capacity at 0.1C and a subsequent jump of 31% at 1C rate is not expected. This may be because of the change in morphology of the particles and increase in the area of bottlenecks along conduction pathways reported in Ti-doped samples facilitating the movement of more Na-ions during cycling thereby increasing capacity and rate

performance. Fig. 4.11(a) shows the rate capability of all five cathodes cycled between 2.00 – 4.25 V at different C-rates in 0.1C - 3C range. While cycling back to lower discharge rates all samples exhibited their initial specific capacities without any significant loss in capacity indicating high reversibility at varying discharge rates. The difference between the discharge specific capacities of x = 0.075 and x = 0 samples was observed to increase with an increase in C-rates. The charge retention capacity of all five samples after 300 cycles at 1C is shown in Fig. 4.11(b). All samples exhibit excellent cyclability with over 95% specific capacity retained after 300 cycles.

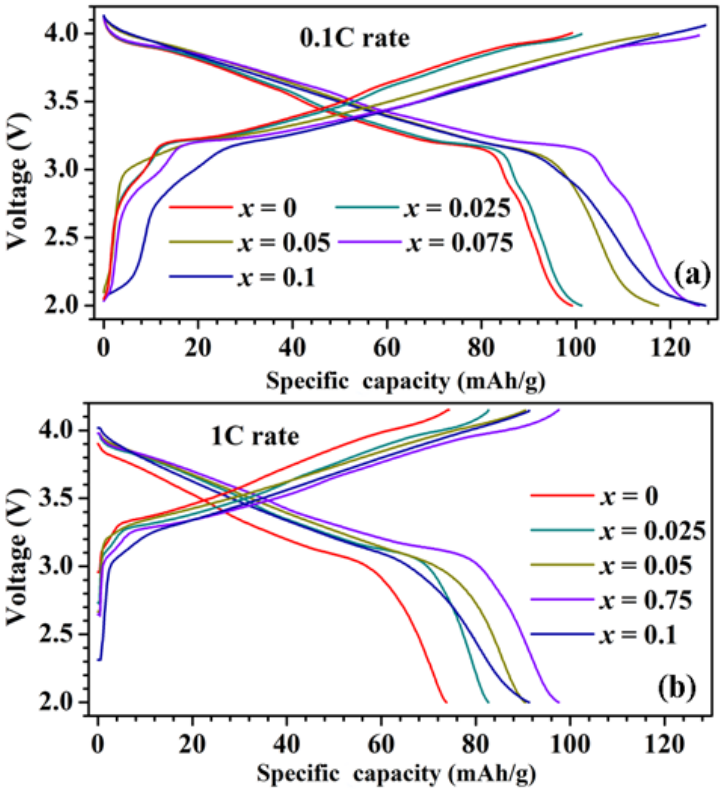

Figure. 4.10. Galvanometric charge-discharge curves at discharge rates of (a) 0.1C and (b) 1C.

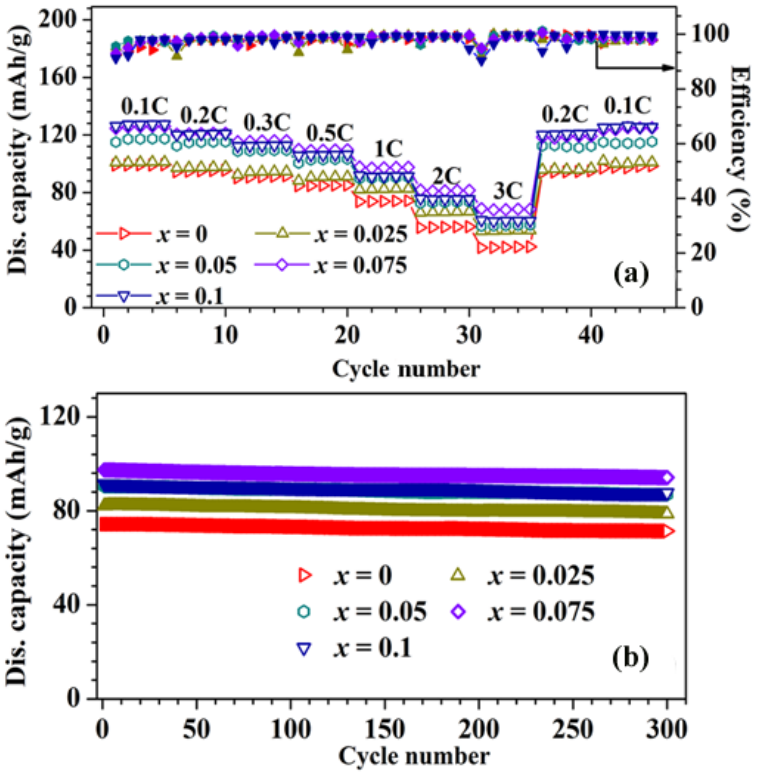

Figure 4.11. (a) The rate capability of the $Na_{0.67}Ni_{0.20}Cu_{0.15}Mn_{(0.65-x)}Ti_xO_2$ samples at different C rates. (b) Cyclic performance of the $Na_{0.67}Ni_{0.20}Cu_{0.15}Mn_{(0.65-x)}Ti_xO_2$ samples when cycled at 1C for 300 cycles.

To study the structural evolution of the cathode materials during Na-ion insertion and extraction, ex-situ XRD was performed on x = 0.075 sample and the result is shown in Fig. 4.12. The XRD plots of both the samples show a gradual shift in the (002) and (004) peaks to lower angles during charging. This is due to an increase in lattice parameters caused by higher repulsion between TM ions during the extraction of Na^+ ions from the material which is reported in other P2 type materials [15, 17, 18]. After discharging these peaks were observed to shift towards their initial positions indicating high reversibility of the intercalation and deintercalation processes and good structural stability of the layered oxide. Apart from the peak shifts reported no new peaks corresponding to phase transformation were observed confirming the existence of a single P2 phase throughout the charging and discharging

process, which could be the reason behind the high cyclic performance of the cathode [15, 18].

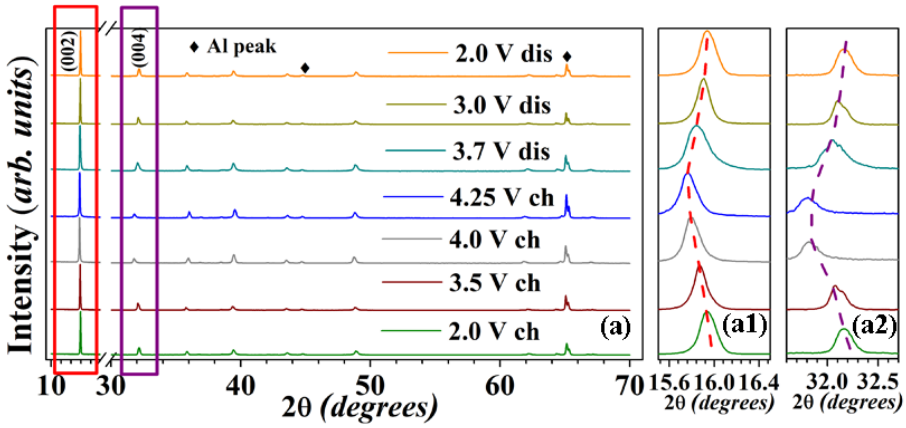

Figure. 4.12. Ex-situ XRD patterns (a) x = 0.075 cathodes during charge(ch)/discharge(dis) cycle at 0.1C with (a1), (a2) showing the magnified view of patterns in the vicinity of (002) and (004) peaks. The Al peaks (marked by ♦ in the Fig. 4.11) belongs to the Al current collector.

4.6. Electrical Properties

To rationalize the improvement in electrochemical performance, the change in electrical properties of the samples was probed by performing complex impedance spectroscopy on the pelletized samples sintered at 900 °C for 12 h. The room temperature Nyquist plots obtained for different samples along with the equivalent circuit used to fit the impedance data are shown in Fig. 4.13. The plots show a decreasing trend in the overall resistance value of the samples with the increase in Ti substitution. Nyquist plots for all samples show a linear tail component in the lower frequency region which is a typical feature of ion-blocking at the sample-electrode interface. Such a feature indicates substantial Na-ion conduction in these samples [19-21]. The values of the total conductivity calculated from the fitted equivalent circuit data for all compositions under investigation are given in Table 4.8.

Table 4.8. Room temperature (RT) conductivity and Na-ion transference number of $Na_{0.67}Ni_{0.20}Cu_{0.15}Mn_{(0.65-x)}Ti_xO_2$ samples

Sample	**RT Conductivity**	**Transference Number (t_{Na})**
$x = 0$	4.03×10^{-6} S/cm	0.86
$x = 0.025$	7.35×10^{-6} S/cm	0.91
$x = 0.050$	1.11×10^{-5} S/cm	0.95
$x = 0.075$	3.07×10^{-5} S/cm	0.97
$x = 0.100$	4.53×10^{-5} S/cm	0.96

To quantify the extent of Na-ion conduction at room temperature in these samples, chronoamperometry was performed under 1 V (Fig. 4.14). The Na-ion transference numbers (t_{Na+}) for different samples obtained from their respective chronoamperometry curves are also provided in Table 4.8. The increasing trend in the conductivity and t_{Na+} values of the Ti substituted samples can be attributed to the increase in the area of lateral faces of the Na – O_6 prisms of the unit cell and the favorable change in the crystal morphology of Ti-substituted samples.

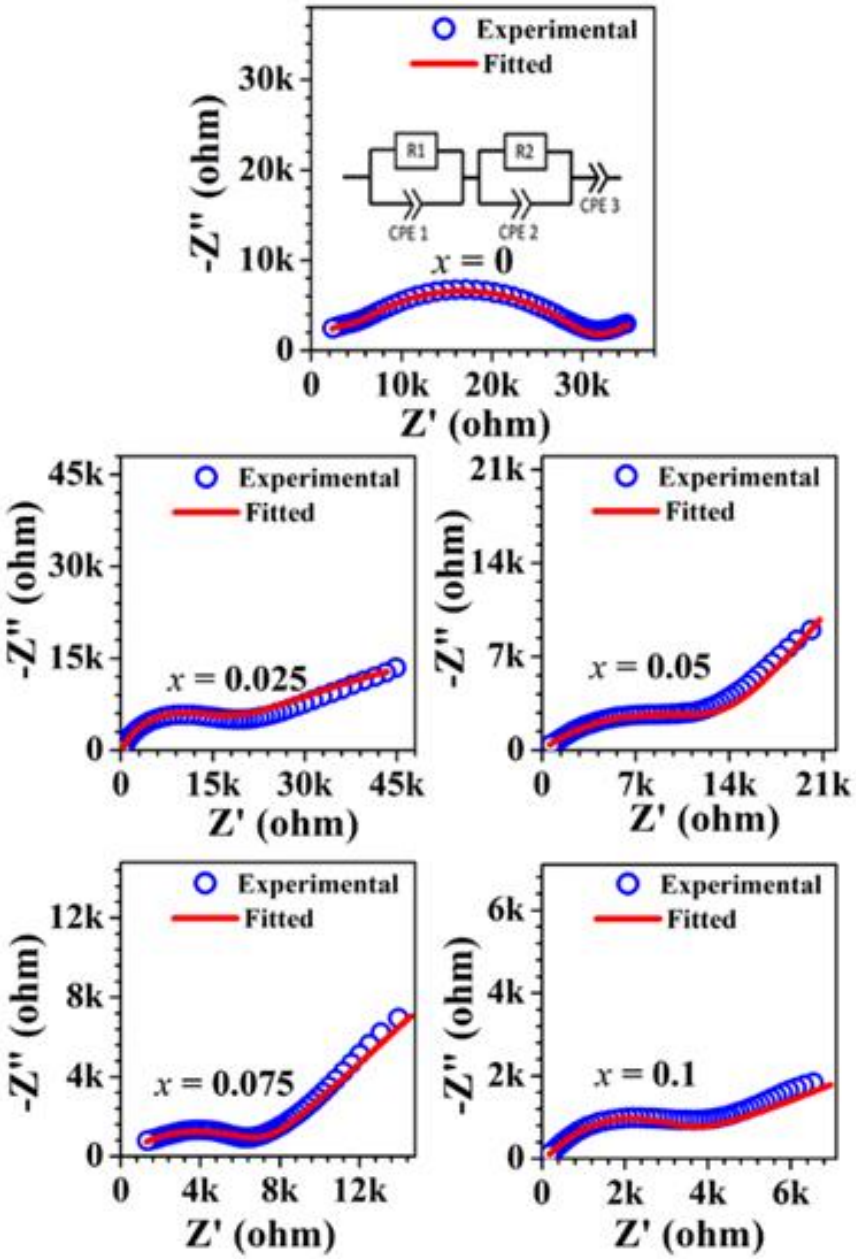

Figure. 4.13. Nyquist plots of various $Na_{0.67}Ni_{0.20}Cu_{0.15}Mn_{(0.65-x)}Ti_xO_2$ compositions at room temperature. The inset shows the equivalent circuit used to fit the impedance data.

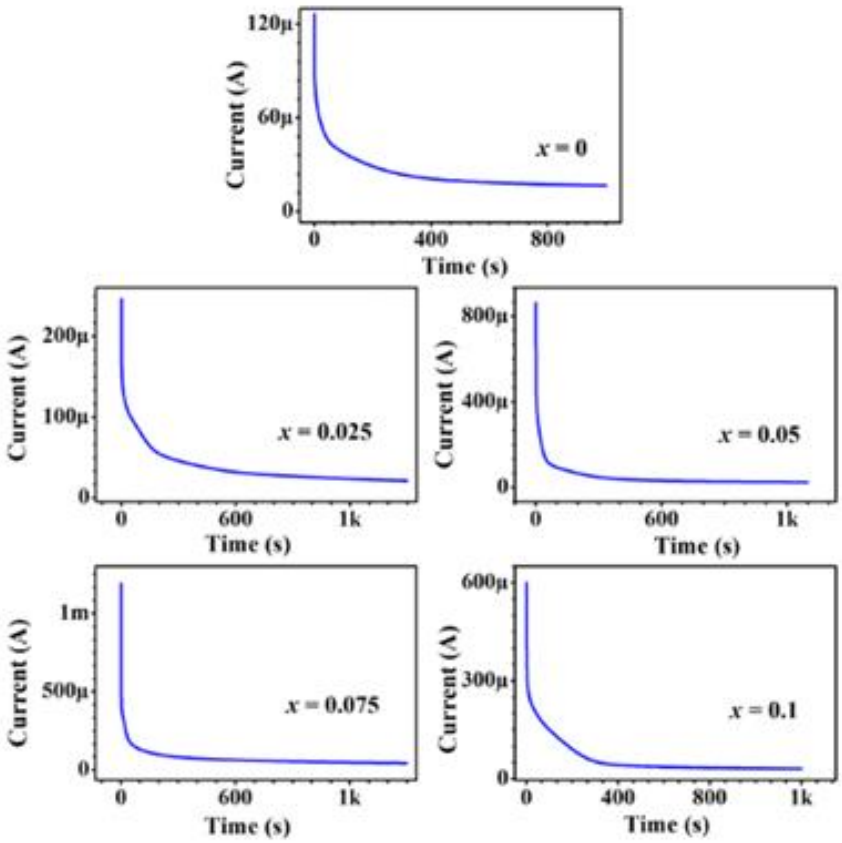

Figure. 4.14. Chronoamperometry curves of $Na_{0.67}Ni_{0.20}Cu_{0.15}Mn_{(0.65-x)}Ti_xO_2$ sample.

The materials were also tested for their moisture stability, for which the powder samples were stored under DI water for 3 h and then dried in a vacuum oven at 100 °C for 5 h. The XRD patterns of the water-treated samples with x = 0, 0.05, and 0.100 are shown in Fig. 4.15. The patterns show no impurity peaks and match with the patterns of their respective as-prepared samples indicating the materials are water and air stable.

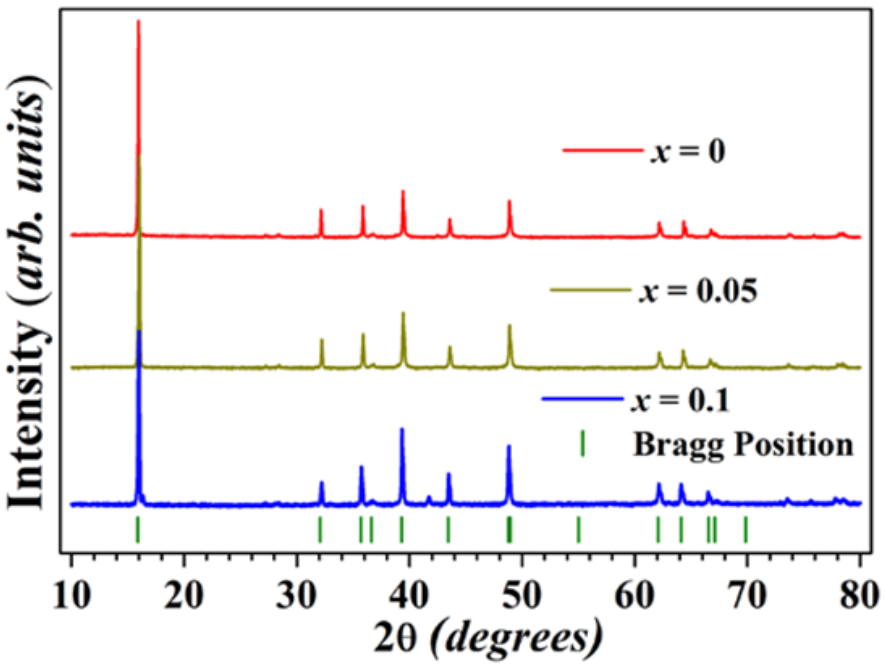

Figure. 4.15. The XRD patterns of the dried powder samples (x = 0, 0.05, and 0.1) after being stored under DI water for 3 h.

4.7. References

[1] P.-F. Wang, H.-R. Yao, X.-Y. Liu, Y.-X. Yin, J.-N. Zhang, Y. Wen, X. Yu, L. Gu, Y.-G. Guo, Science Advances, 4 (2018) eaar6018.

[2] D.H. Lee, J. Xu, Y.S. Meng, Physical Chemistry Chemical Physics, 15 (2013) 3304-3312.

[3] R. Berthelot, D. Carlier, C. Delmas, Nature Materials, 10 (2011) 74-80.

[4] A. Gutierrez, W.M. Dose, O. Borkiewicz, F. Guo, M. Avdeev, S. Kim, T.T. Fister, Y. Ren, J. Bareño, C.S. Johnson, The Journal of Physical Chemistry C, 122 (2018) 23251-23260.

[5] A.J. Toumar, S.P. Ong, W.D. Richards, S. Dacek, G. Ceder, Physical Review Applied, 4 (2015) 064002.

[6] K. Tang, Y. Huang, X. Xie, S. Cao, L. Liu, H. Liu, Z. Luo, Y. Wang, B. Chang, H. Shu, X. Wang, Chemical Engineering Journal, 399 (2020) 125725.

[7] Q. Pei, M. Lu, Z. Liu, D. Li, X. Rao, X. Liu, S. Zhong, ACS Applied Energy Materials, 5 (2022) 1953-1962.

[8] J.-k. Park, G.-g. Park, H.H. Kwak, S.-T. Hong, J.-w. Lee, ACS Omega, 3 (2018) 361-368.

[9] R. Shannon, Acta Crystallographica Section A, 32 (1976) 751-767.

[10] K. Momma, F. Izumi, Journal of Applied Crystallography, 44 (2011) 1272-1276.

[11] W. Kang, D.Y.W. Yu, P.-K. Lee, Z. Zhang, H. Bian, W. Li, T.-W. Ng, W. Zhang, C.-S. Lee, ACS Applied Materials & Interfaces, 8 (2016) 31661-31668.

[12] J.F. Moulder, J. Chastain, Handbook of X-ray Photoelectron Spectroscopy: A Reference Book of Standard Spectra for Identification and Interpretation of XPS Data, Physical Electronics Division, Perkin-Elmer Corporation, 1992.

[13] S. Hüfner, Photoelectron spectroscopy: principles and applications, Springer Science & Business Media, 2013.

[14] L. Wang, Y.-G. Sun, L.-L. Hu, J.-Y. Piao, J. Guo, A. Manthiram, J. Ma, A.-M. Cao, Journal of Materials Chemistry A, 5 (2017) 8752-8761.

[15] L. Yang, S.-h. Luo, Y. Wang, Y. Zhan, Q. Wang, Y. Zhang, X. Liu, W. Mu, F. Teng, Chemical Engineering Journal, 404 (2021) 126578.

[16] M.H. Han, E. Gonzalo, N. Sharma, J.M. López del Amo, M. Armand, M. Avdeev, J.J. Saiz Garitaonandia, T. Rojo, Chemistry of Materials, 28 (2016) 106-116.

[17] X. Wu, G.-L. Xu, G. Zhong, Z. Gong, M.J. McDonald, S. Zheng, R. Fu, Z. Chen, K. Amine, Y. Yang, ACS Applied Materials & Interfaces, 8 (2016) 22227-22237.

[18] X.-H. Zhang, W.-L. Pang, F. Wan, J.-Z. Guo, H.-Y. Lü, J.-Y. Li, Y.-M. Xing, J.-P. Zhang, X.-L. Wu, ACS applied materials & interfaces, 8 (2016) 20650-20659.

[19] A.R.C. Bredar, A.L. Chown, A.R. Burton, B.H. Farnum, ACS Applied Energy Materials, 3 (2020) 66-98.

[20] L.A. Middlemiss, A.J.R. Rennie, R. Sayers, A.R. West, Energy Reports, 6 (2020) 232-241.

[21] N. Meddings, M. Heinrich, F. Overney, J.-S. Lee, V. Ruiz, E. Napolitano, S. Seitz, G. Hinds, R. Raccichini, M. Gaberšček, J. Park, Journal of Power Sources, 480 (2020) 228742.

Conclusions and Future Scope of Work

5.5. Conclusions

In summary, $Na_{0.70}Ni_{0.20}Cu_{0.15}Mn_{0.65}O_2$ (NNCM) was successfully synthesized using a sol-gel route. Rietveld refinement of the powder XRD data shows a single P2 phase with a hexagonal lattice ($P6_3/mmc$ space group). SEM analysis of the powder sample shows hexagon-like plates with an average particle size of ~ 2 μm. Elemental mapping confirmed the uniform distribution of the constituent elements throughout the sample. Impedance measurements suggest the conductivity of Na-ions in NNCM ceramics is greatly influenced by the highly resistive grain boundaries. The conductivity of grain boundaries was found to be about 4.7×10^{-6} Scm^{-1} while that of the grains was around 5.25×10^{-5} Scm^{-1} at room temperature. The values of activation energies (E_A) were found to be 0.22 ± 0.01 eV for grain boundary conduction, 0.189 ± 0.008 eV for grain conduction, and 0.21 ± 0.01 eV for overall conduction in NNCM ceramic sample. Chronoamperometry and dielectric response establish the dominance of Na-ions in the overall conduction of this material. The material showed a specific capacity of 99 mAh/g and 74 mAh/g at 0.1C and 1C, respectively, with 95% of its initial capacity retained after 300 cycles at 1C.

To further improve performance characteristics of the material, a series of samples where Mn^{4+} in NNCM was substituted with Ti^{4+} in varying concentrations (NNCMT-*x*, x = 0, 0.025, 0.050, 0.075, and 0.100) were also synthesised. Analysis of XRD patterns and FESEM images of the showed improvements in the size of conduction bottlenecks along with the successful suppression of Na-ion vacancy ordering in Ti substituted samples. An improvement in Na-ion diffusion in Ti-doped samples was evidenced by the increase in ionic conductivity and Na-ion transference number. On cycling between 2 – 4.25 V, x = 0.075 sample showed the highest specific capacity of 127 mAh/g at 0.1C which is about 27% higher than that for the undoped sample. Even at higher discharge rate of 1C, $Na_{0.70}Ni_{0.20}Cu_{0.15}Mn_{0.575}Ti_{0.075}O_2$ showed a

capacity of 97 mAh/g as compared to 74 mAh/g that of the $x = 0$ sample. Further, this sample retained more than 95% of its initial capacity after 300 cycles at 1C. Apart from exhibiting an improved specific capacity, excellent cyclability, and good rate performance, $Na_{0.70}Ni_{0.20}Cu_{0.15}Mn_{0.575}Ti_{0.075}O_2$ was found to be stable in moisture making it an attractive candidate as a Na-ion battery cathode.

5.2. Future Scope of Work

- The study could be extended further using the hard carbon as the anode to move a step towards the commercialization.
- The mass loading of active material on the current collector used for evaluating the electrochemical performance in this study was ~ 2 mg/cm^2. This should be further increased to 20 mg/cm2 (on both side of the current collector) in order to study the effect of mass loading on the electrochemical behaviour especially at fast discharging rates. The observed high sodium conduction in Ti substituted samples should results in much better specific capacity and resultant high power density as compared to the parent material.
- Postmortem analysis of the cells using EIS, ex-situ XRD, and SEM can be used to investigate the failure mechanisms that causes capacity fading in these cells.
- The electrochemical behaviour for these materials should be further explored in the different voltage windows in the 1.5 - 4.50 V ranges. Such studies would help in analyzing the effect of Ti^{4+} ions in alleviating the phase changes and structural distortions at higher and lower voltages. It is important to note that in layered oxides, some structural changes cause capacity fading.
- For the sample containing optimum Ti concentration, the Na-ion content in the composition could be varied to develop the extensive *composition - synthesis temperature - property* relationship. It would be interesting to see if the Ti doping

could help in stabilizing the P2-type phase with even higher Na concentration i.e., ; $x > 0.8$ in Nax(TM)O_2.

- The effect of morphology on the electrical and electrochemical properties with Ti substitution has been reported in this study. The effect of different morphologies attained using various synthesis techniques can be explored to further improve performance.
- Finally, the work should be scaled up from fabricating coin cells to pouch cells with higher active cathode material loading to realize its potential for commercialization.